A SOFTWARE CONTROLLED POLARIZATION AND PATTERN RECONFIGURABLE MICROSTRIP PARASITIC ARRAY ANTENNA FOR A MARKET MEDIATED SOFTWARE DEFINED COMMUNICATIONS SYSTEM

A Thesis

by

ABHAY SHANKAR ANAND

Submitted to the Office of Graduate and Professional Studies of
Texas A&M University
in partial fulfillment of the requirements for the degree of

MASTER OF SCIENCE

Chair of Committee,	Gregory H. Huff
Committee Members,	Robert D. Nevels
	Jean-Francois Chamberland
	Sheng-Jen Hsieh
Head of Department,	Miroslav M. Begovic

December 2017

Major Subject: Electrical Engineering

ABSTRACT

Software Defined Radio (SDR) provides a platform for a reconfigurable communication system that is solely controlled by a software program with access to certain hardware modules. SDRs are typically connected to very minimalistic, and often, manually controlled reconfigurable antenna(s) with no software control over radiation parameters. Hence, on a wave propagation front, the radiator does not capitalize on the software infrastructure it is connected to. This thesis presents a software controlled pattern and polarization reconfigurable microstrip patch antenna, with reconfigurable parasitic elements, for reconfigurable wireless networks and applications.

The antenna is designed to operate from 2.4 GHz to 2.5 GHz, covering all channels (channels 1 through 14) of the 2.4 GHz ISM band. This broadband behavior is achieved with a two-layer stacked annular ring patch antenna, separated by a layer of foam. This antenna is dual probe-fed to achieve vertical and horizontal linear polarizations as well as right-hand and left-hand circular polarizations. Pattern reconfiguration is achieved with a third layer composed of microstrip patch elements acting as parasitic radiators, either reflecting or directing a beam in a direction, which are controlled by RF PIN diodes. Elements are placed such that pattern reconfiguration is possible across all polarization modes.

Various iterations of the design process are discussed along with their issues and solutions. Other reconfiguration techniques are also suggested as part of future work.

ACKNOWLEDGEMENTS

I thank my advisor, Dr. Gregory Huff, for his guidance, support and for providing all the resources necessary to complete this research work. I would also like to thank my committee members Dr. Robert Nevels, Dr. Jean-Francois Chamberland and Dr. Sheng-Jen Hsieh for their time to review this work.

I am eternally thankful to my undergraduate electromagnetics professor, Sabarish Narayanan B., for helping me steer my path towards this field and to further help mold this interest into a more focused study. I would also like to thank my undergraduate advisor, Dr. Shanmugha Sundaram G. A., and Dr. Jayakumar M. who have both been monumental in building my foundations in this field.

A huge thanks goes to all my colleagues and friends in the Huff Research Group lab, especially Francisco Espinal for his support in fabrication and measurements, Shih-Yuan "Steven" Yeh for his massive wealth of knowledge, Sumana Pallampati and Amrita Bal for their thoughts and inputs at various stages of this work, Daniel Carey for helping out with all the hardware and equipment in the lab, Joshua Ruff for his coding and circuitry skills, and Zhong Chen for giving me the motivation and strength to work harder and for critiquing my work.

I also extend my gratitude to my close friends Shanmathi Mookiah, Ashok Shanker, Nagaraj Janakiraman and Kartic Bhargav who have been a good company and I have enjoyed the many night-long thought-provoking conversations. Thanks also to the team of SPICMACAY TAMU and to Dr. Krishna Narayanan, Dr. Shankar

Bhattacharyya, and Dr. N. Sivakumar for giving me the opportunity to enjoy music and also feel terribly homesick.

A huge thanks to my parents and brother for their love and encouragement and finally to the Almighty who opens the right doors at the right time, guiding me constantly.

CONTRIBUTORS AND FUNDING SOURCES

Contributors

This work was supervised by a thesis committee consisting of Professor Gregory Huff (advisor), Professor Robert Nevels and Professor Jean-Francois Chamberland of the Department of Electrical and Computer Engineering and Professor Sheng-Jen Hsieh of the Department of Engineering Technology and Industrial Distribution.

All work for this thesis was completed independently by the student.

Funding Sources

There are no outside funding contributions to acknowledge related to the research and compilation of this document.

NOMENCLATURE

ARMSP	Annular Ring Microstrip Patch Antenna
CAD	Computer Aided Design
DC	Direct Current
GUI	Graphical User Interface
IDE	Integrated Development Environment
ISM	Industrial, scientific and medical
PEC	Perfect Electric Conductor
PIN	P-type, Intrinsic layer, N-type
PMC	Perfect Magnetic Conductor
QWT	Quarter Wave Transformer
RF	Radio Frequency
SDR	Software Defined Radio
TEM	Transverse Electric and Magnetic
TM	Transverse Magnetic

TABLE OF CONTENTS

Page

ABSTRACT ii

ACKNOWLEDGEMENTS iii

CONTRIBUTORS AND FUNDING SOURCES v

NOMENCLATURE vi

TABLE OF CONTENTS vii

LIST OF FIGURES ix

LIST OF TABLES xii

CHAPTER I INTRODUCTION AND MOTIVATION 1

CHAPTER II BACKGROUND 4

2.1 Two-Port Network Analysis 4
2.2 Rectangular Microstrip Patch Antennas 6
2.2.1 Cavity Model Analysis of Rectangular Patch Antenna 7
2.3 Annular Ring Patch Antenna and Cavity Model Analysis 9
2.4 Yagi-Uda Antenna Array 14
2.5 RF Diodes 16

CHAPTER III DESIGN OF A POLARIZATION RECONFIGURABLE BROADBAND ANNULAR RING PATCH ANTENNA 19

3.1 Single Layer Annular Ring Patch (ARMSP) Antenna 19
3.2 Stacked ARMSP Antenna 24
3.3 Polarization Reconfiguration on Stacked ARMSP Antenna 27
3.4 Polarization Reconfigurable Stacked ARMSP Antenna on Duroid 5870 Substrate 31

CHAPTER IV DESIGN OF A PATTERN RECONFIGURABLE BROADBAND ANNULAR RING PATCH ANTENNA 34

4.1 Quasi-Yagi Coupled Stacked ARMSP Antenna 34
4.1.1 Effect of a Director on the Stacked ARMSP Antenna 34

4.1.2 Effect of Adding a Foam Layer between the Stacked ARMSP and Yagi-Elements 38
4.1.3 Effect of Introducing Reflector Element 38
4.1.4 Effect of Increasing Foam Thickness ($t4$) between Stacked ARMSP Antenna and Yagi-Elements 40
4.2 Pattern Reconfigurable Quasi-Yagi Coupled Stacked ARMSP Antenna 43
4.2.1 Use of RF PIN Diodes to Switch between Director and Reflector 43
4.2.2 Impedance Matching the Quasi-Yagi Pattern Reconfigurable Stacked ARMSP Antenna 47

CHAPTER V IMPROVEMENTS ON PATTERN RECONFIGURABLE BROADBAND ANNULAR RING PATCH ANTENNA 51

5.1 Improving Radiating Element Broadband Response on Duroid 5870 Substrate 51
5.2 Design of DC Lines for RF PIN Diode Biasing 56
5.2.1 First Iteration with RF Open-Circuit Cross-Coupled Lines 56
5.2.2 Second Iteration with Meandering DC Feed Lines 57
5.3 Antenna Fabrication and Measurements 60
5.3.1 Fabricated Stacked Patch Antenna with Meandering DC Feed Lines 60

CHAPTER VI SOFTWARE CONTROL MECHANISM 66

6.1 System Block Diagram and Working Principle 66
6.2 Proof-of-Concept Design and Integration with Reconfigurable SDR 68
6.3 Bias Network Integration with the Reconfigurable ARMSP Antenna 70

CHAPTER VII FUTURE WORK AND CONCLUSIONS 72

REFERENCES 73

LIST OF FIGURES

Page

Fig. 1. Two-port network illustrating network parameters. 5

Fig. 2. Rectangular Microstrip patch antenna with the patch and substrate surfaces along x-y plane and z-axis pointing upwards. 6

Fig. 3. Fringing electric fields along the length of the patch responsible for radiation. 8

Fig. 4. Annular Ring patch geometry and design variables. 10

Fig. 5. Cavity model of Annular Ring patch showing PEC and PMC walls (ground plane not shown). 11

Fig. 6. Yagi-Uda Linear Antenna Array Configuration. 15

Fig. 7. PN junction diode is formed by fusing P-type and N-type semiconductors. Depletion region formed around the junction giving rise to an electric field...17

Fig. 8. Analytical and simulated input impedances of TM_{11} mode of annular ring patch antenna. 21

Fig. 9. Input impedance of simulated single layer ARMSP antenna showing initial design (a=11mm, b=22mm) vs. optimized design (a=9mm, b=20mm). 22

Fig. 10. Reflection coefficient of single layer ARMSP antenna – comparison between 50Ω and 550Ω coaxial feed line. Impedance bandwidth ≈0.9%. 23

Fig. 11. Normalized radiation pattern of single layer ARMSP antenna at 2.45 GHz. 23

Fig. 12. HFSS 3D model cut-out of the stacked ARMSP antenna; a_2 and b_2 are the inner and outer radii, respectively, of the stacked patch element, t_1, t_2 and t_3 denote the thickness of the first layer substrate, foam and second layer substrate, respectively. 25

Fig. 13. Effect of varying foam thicknesses on the reflection coefficient and impedance bandwidth of a stacked ARMSP antenna. 26

Fig. 14. Normalized radiation pattern for a stacked ARMSP antenna with $t_2 = 5.5mm$, at 2.45 GHz. 27

Fig. 15. Illustration of a dual feed ARMSP giving rise to horizontal and vertical linear polarizations in TM_{11} mode. Vertical polarization is observed along the xz-plane and horizontal polarization, along the yz-plane. 28

Fig. 16. S-parameters of the dual feed stacked ARMSP antenna; both ports are matched across the desired bandwidth and there is high isolation between them. 29

Fig. 17. Normalized radiation patterns for vertical and horizontal linear polarizations of stacked ARMSP antenna. 30

Fig. 18. Normalized radiation patterns showing right-hand and left-hand circular polarizations. 31

Fig. 19. S-parameters of the dual feed stacked ARMSP antenna with Duroid 5870 substrates. The impedance bandwidth achieved is approximately 11%. 33

Fig. 20. Stacked ARMSP antenna with parasitic element (director) for beam-steering; w_D is the width of the director and $spacing_D$ is the spacing of the director from the center of the second layer ARMSP. 35

Fig. 21. Port reflection parameters for $w_D = 16mm$ and $spacing_D = 46mm$. 36

Fig. 22. Normalized radiation patterns showing about $20°$ of beam tilt towards negative axis. The patterns along vertical polarization plane remains unaltered. 37

Fig. 23. Port reflection parameters for different values of foam thicknesses ($t_2 = 3mm\ to\ 5.5mm$). The final value chosen at this stage was $t_2 = 3.5mm$. 39

Fig. 24. HFSS 3D model, depicting a foam layer that separates the Yagi-elements and the stacked ARMSP antenna. The shorter element (towards the right) is the director and the longer element (towards the left) is the reflector. 40

Fig. 25. Port reflection parameters showing acceptable impedance matching across the desired bandwidth and strong isolation between the two feed ports. 42

Fig. 26. Normalized radiation pattern showing fields for horizontal polarization 42

Fig. 27. RF PIN Diode configuration on the Yagi-elements to control lengths of those elements. Y_1 and Y_3 couple with feed port 2 and Y_2 and Y_4 couple with feed port 1. 44

Fig. 28. Port reflection parameters for all Yagi modes affecting port 2. 45

Fig. 29. Normalized radiation patterns for all Yagi modes affecting port 2. 46

Fig. 30. Illustration of a Circular disk loaded Quasi-Yagi Pattern Reconfigurable Stacked ARMSP antenna. 48

Fig. 31. Port reflection parameters for all modes on Y_1 and Y_3, when excited by port 2. 49

Fig. 32. Normalized radiation patterns for design with the circular disk loading for all Yagi modes. 50

Fig. 33. Illustration of design of the third patch element (as a replacement to the circular disk). 53

Fig. 34. Port reflection parameters for the third patch element as a cross structure. Shown are all modes on Y1 and Y3 when excited by port 2. 54

Fig. 35. Normalized radiation patterns for design with crossed microstrip line loading for all Yagi modes. 55

Fig. 36. Design of the DC feed lines. 56

Fig. 37. Design illustrating meandering feed lines and RF chokes. 58

Fig. 38. Port reflection parameters for the meandering DC feed lines design. All modes are sufficiently well matched. 58

Fig. 39. Normalized radiation patterns of antenna with meandering DC feed lines. 59

Fig. 40. Fabricated version of the meandering DC feed line top layer 60

Fig. 41. Normalized radiation patterns of meandering DC feed lines Measured vs. Simulated. 61

Fig. 42. CAD model of tri-state Yagi-elements with diode configurations illustrated. ... 62

Fig. 43. Fabricated version of the meandering DC feed lines with tri-state Yagi-elements. 63

Fig. 44. Port reflection parameters comparing simulated data vs. measured. 64

Fig. 45. Normalized radiation patterns of the tri-state Yagi-elements, simulated vs. measured. 65

Fig. 46. Block diagram of software control mechanism for reconfigurable antenna. 67

Fig. 47. Screenshot of software program depicting an auto-switching of polarization states to that of the router. 69

Fig. 48. Screenshot of the modified version of the software program for the reconfigurable ARMSP antenna. 70

LIST OF TABLES

Page

Table 1. Comparison of analytical and CAD simulations against calculated and measured data presented in [8]. 20

Table 2. Optimized design parameters for Stacked ARMSP Antenna on Duroid 5870 substrate. 32

Table 3. Design parameters for Quasi-Yagi Stacked ARMSP antenna with a Director-Reflector configuration 41

Table 4. Design parameters for pattern reconfigurable Quasi-Yagi Stacked ARMSP Antenna with broadband characteristics and improved reflection coefficients. 52

CHAPTER I

INTRODUCTION AND MOTIVATION

A Market-Mediated SDR is a software-defined communication system with a certain type of cognitive response to users' network utilization pattern; competition for common resources; and a real-time demand of data packets for various applications across multiple users. At the same time, the system maintains optimal performance for each user. As described in [1], the communication system performs a per-packet level switching, at sub-millisecond rates, requiring pattern and polarization reconfiguration at the antenna-front. The antenna used in [1] is a polarization reconfigurable microstrip antenna with solid-state (RF PIN diode) switching [2], [3]. Solid-state switching was preferred over the fluidic switching mechanism due to the limitation on switching speeds.

Polarization reconfigurable antennas, in this communication system, allow the router to orient its polarization to that of a targeted user for a transmitted/received packet at a specific moment in time. It also allows frequency re-use by having two channels transmit/receive at two polarizations with very low interference due to the innate orthogonality between them. Pattern reconfigurable antennas, on the other hand, can direct radiation towards an intended user and boost signal strength between the router and user, thereby reducing latency times and dropped packets; thus, steering away from noise [4]. Traditionally, pattern reconfigurable antennas comprise of multiple antennas

forming a phased array system. This system requires multiple antennas and complex phasing mechanism that occupy large space (of the order of a few wavelengths).

A polarization and pattern reconfigurable antenna presented in this thesis is intended to replace the above-mentioned antenna [2], [3], thus providing the system with an added degree of control over the communication between users and the router. Pattern reconfiguration is achieved with the help of parasitic array elements, similar to that discussed in [5], and polarization reconfiguration is achieved with dual-feed orthogonal excitation of the microstrip patch antenna. The antenna is designed to operate within all the fourteen channels of the 2.4 GHz Wi-Fi ISM band. To achieve this relatively broadband behavior, a stacked annular ring microstrip patch antenna (ARMSP) is designed with orthogonal dual-feeds, designed to operate at TM_{11} mode and is integrated with a novel parasitic array which provides beam-steering pattern reconfiguration without the need for any phase-shifting mechanism or additional RF signal.

Chapter 2 discusses the background required for this thesis and the theory behind the design of the antenna using a cavity model approach. The operation of a Yagi-Uda antenna is also presented to aid the understanding of the beam-steering mechanism used in the antenna under study.

Chapter 3 presents the broadband characteristics of the radiating element and the design stages involved.

Chapter 4 presents the first iteration of the radiating element coupled with the parasitic beam-steering array and the need for further improvements.

Chapter 5 discusses the next stages of iterations with most of the issues accounted for and a field-deployable version of the antenna under study.

Chapter 6 discusses future work and enhancement of the design of the antenna for a more compact version with fewer solid-state devices, thus increasing the overall efficiency of the antenna.

CHAPTER II

BACKGROUND

2.1 Two-Port Network Analysis

Every antenna is characterized by the amount of power that it transmits (in the case of a transmitting antenna) and therefore the amount of power that is reflected to the source, which is detrimental to the entire system. This is studied with the help of a single or multi-port network analysis [6]. For the purposes of this thesis, since the antenna is designed with a dual-feed, the analysis is limited to a two-port network.

Since voltages, currents, and impedances cannot be measured directly at microwave frequencies, these quantities must be derived using more directly measurable quantities such as the amplitude and phase angles of reflected waves with respect to the amplitude and phase angles of incident waves. This relation between reflected (scattered) and incident waves is represented mathematically by a matrix called Scattering matrix or Scattering parameters.

Consider a two-port network as shown in Fig. 1, where a_1 and b_1 are the incident and reflected waves, respectively, at port 1 and a_2 and b_2 are the incident and reflected waves, respectively, at port 2.

With these network parameters, the S parameters are defined as follows:

$$S_{11} = \left.\frac{b_1}{a_1}\right|_{a_2=0} \qquad S_{12} = \left.\frac{b_1}{a_2}\right|_{a_1=0}$$
$$S_{21} = \left.\frac{b_2}{a_1}\right|_{a_2=0} \qquad S_{22} = \left.\frac{b_2}{a_2}\right|_{a_1=0} \tag{2.1}$$

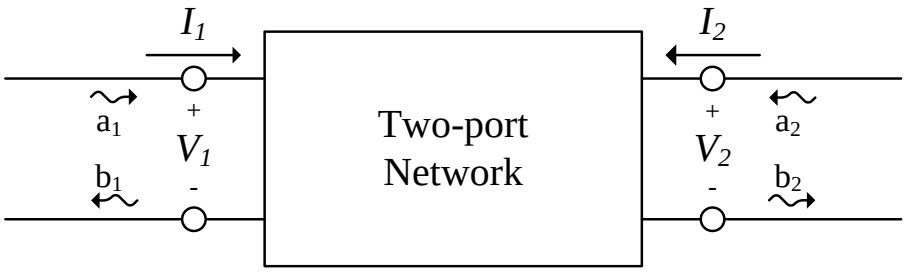

Fig. 1. Two-port network illustrating network parameters.

where $a_n = 0$ means that the incident wave at port n has zero amplitude, which implies zero input power. In the form of a matrix, the relation between reflected and incident waves are given as

$$\begin{bmatrix} b_1 \\ b_2 \end{bmatrix} = \begin{bmatrix} S_{11} & S_{12} \\ S_{21} & S_{22} \end{bmatrix} \begin{bmatrix} a_1 \\ a_2 \end{bmatrix} \tag{2.2}$$

In general, the S parameters (S_{mn}) are interpreted as effect on port m due to port n. With this interpretation, S_{11} and S_{22} are termed as reflection coefficients at port 1 and port 2 respectively; S_{21} and S_{12} are the transmission coefficients from port 1 to port 2 and vice-versa respectively. Since the S parameters are a ratio, they lie within the range $[0,1]$. To easily relate the S parameters with respect to power, they are represented in decibels (dB) as

$$\left|S_{mn}\right|_{dB} = 20\log\left|S_{mn}\right| \tag{2.3}$$

A general rule of thumb followed with respect to S parameters and microwave devices is that input/output reflection coefficient should be $< -10\text{dB}$, or in other words, reflected power should be less than approximately 10% of the input/output power. For the purposes of this thesis, bandwidth of a certain device is calculated for reflection coefficients $< -10\text{dB}$.

2.2 Rectangular Microstrip Patch Antennas

Microstrip patch antennas are comprised of a thin metallic strip/patch placed on top of a metallic ground plane, separated by a dielectric material of a certain thickness. Microstrip patch antennas are low profile, planar, relatively inexpensive, and easy to manufacture, making them perfect choices for mobile telecommunication devices [7].

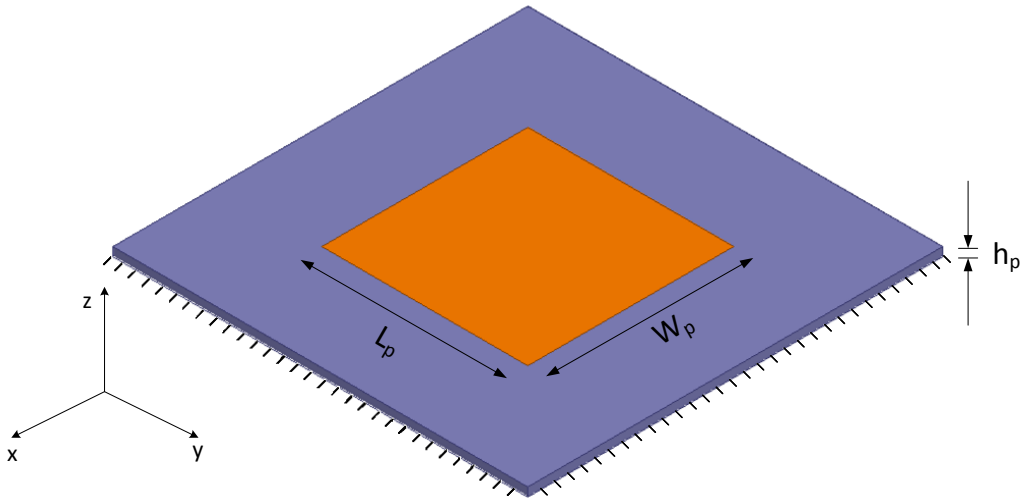

Fig. 2. Rectangular Microstrip patch antenna with the patch and substrate surfaces along x-y plane and z-axis pointing upwards.

The substrate properties are typically characterized into relative permittivity (ϵ_r) and relative permeability (μ_r). For a rectangular patch antenna, as shown in Fig. 2, the substrate parameters, also including substrate thickness (h_p), along with the length (L_p) and width (W_p) of the patch determine the radiation characteristics. A rectangular patch antenna has a narrow bandwidth (around 1 – 3 %) of resonance, which is a function of L_p, W_p, and h_p, depending on the mode of excitation. These modes can be analyzed using either transmission line model or cavity model; and for the purposes of this thesis, cavity model approach is described.

2.2.1 Cavity Model Analysis of Rectangular Patch Antenna

A microstrip patch antenna can be modelled as a dielectric loaded cavity with perfect electric conductors (PEC) on the top and bottom walls and perfect magnetic conductors (PMC) along the perimeter of the patch – modelling the perimeter walls as PMC simulates an ideal open circuit between the top and bottom PEC [7]. In the case of a rectangular patch, the four side PMC walls represent four narrow slots, which are responsible for radiation. All the six walls of this cuboidal cavity have surface currents, which are comprised of electric and magnetic current densities. As explained in [7], the electric current densities on the top and bottom faces (PEC) are negligible and are set to zero. The side PMC walls, however, bear magnetic current densities ($\mathbf{M}_s$) and is doubled in magnitude due to the presence of a ground plane. The expression is given as follows:

$$\mathbf{M}_s = -2\hat{\mathbf{n}} \times \mathbf{E}_a \tag{2.4}$$

where $\mathbf{E}_a$ represents the electric field at the slots. The resonant frequencies for this cavity can be given by [7]:

$$(f_r)_{mnp} = \frac{1}{2\pi\sqrt{\mu\epsilon}}\sqrt{\left(\frac{m\pi}{h_p}\right)^2 + \left(\frac{n\pi}{L_p}\right)^2 + \left(\frac{p\pi}{W_p}\right)^2} \tag{2.5}$$

where m, n, and p represent the number of half-cycle field variations along z, x, and y axes respectively.

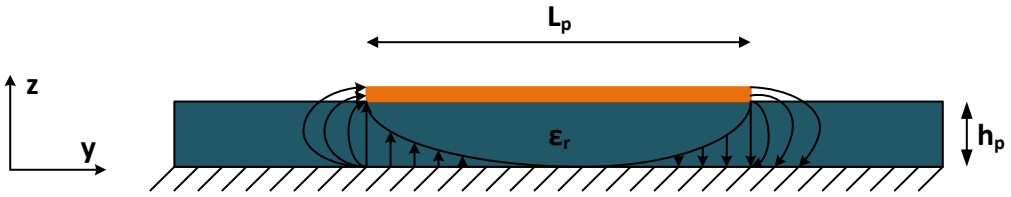

Fig. 3. Fringing electric fields along the length of the patch responsible for radiation.

Assuming the dominant mode (TM_{010}) within the cavity, of the four slots, only two radiate while the other two cancel out the other. It is a considered general practice to represent the separation between the two radiating slots as L_p and the two non-radiating slots as W_p. The radiation pattern of this patch can, therefore, be calculated as a linear array of two magnetic dipoles with current densities given by (2.4). These fields emanating from the two radiating slots are called fringing fields (Fig. 3) and, as mentioned earlier, are responsible for radiation. Because of these fringing fields, the patch looks electrically larger than its physical length and hence should be accounted for in the design. The non-homogeneity in the dielectric media involved in these fields

reduce the overall dielectric constant (assuming that the media around the patch is air with $\epsilon_r = 1$), giving rise to a term generally called effective dielectric constant, which is given by:

$$\epsilon_{reff} = \frac{\epsilon_r + 1}{2} + \frac{\epsilon_r - 1}{2}\left[1 + \frac{12h_p}{W_p}\right]^{-\frac{1}{2}} \tag{2.6}$$

2.3 Annular Ring Patch Antenna and Cavity Model Analysis

Consider an annular ring patch antenna as shown in Fig. 4. It has an inner radius a and an outer radius b, sitting atop a substrate of thickness h, with a dielectric constant ϵ_r. In the cavity model, similar to the rectangular patch discussed earlier, the dielectric loaded cavity is surrounded by PEC walls in the top and bottom and PMC walls on the sides. Here, however, there would be two PMC walls, along the interior and exterior of the annulus, as shown in Fig. 5. The resonant frequencies inside this cavity are determined by [8]:

$$f_{mn} = \frac{k_{mn}c}{2\pi\sqrt{\epsilon_{eff}}} \tag{2.7}$$

Here, k_{mn} are the roots of the characteristic equation [9]:

$$\frac{\mathrm{J}_{\mathrm{n}}^{'}(k_{mn}a)}{\mathrm{N}_{\mathrm{n}}^{'}(k_{mn}a)} = \frac{\mathrm{J}_{\mathrm{n}}^{'}(k_{mn}b)}{\mathrm{N}_{\mathrm{n}}^{'}(k_{mn}b)} \tag{2.8}$$

Here, $\mathrm{J}_{\mathrm{n}}^{'}(x)$ is the first derivative of n^{th} order Bessel function of the first kind and $\mathrm{N}_{\mathrm{n}}^{'}(x)$ is the first derivative of n^{th} order Bessel function of the second kind (also called

Neumann function). The derivatives are taken with respect to $k\rho$. To analyze the fields inside the cavity, [9] has introduced a representation by expansion in resonant modes. Here, the wave equation in the cavity with a z directed current is given as:

$$\left(\nabla^2 + k^2\right) E_z = j\omega\mu \mathbf{J} \bullet \hat{\mathbf{z}} \tag{2.9}$$

Here, E_z, is represented in terms of resonant modes ψ_m as:

$$E_z = j\omega\mu \sum_m \frac{1}{k^2 - k_m^2} \frac{\langle J\psi_m \rangle}{\langle \psi_m \psi_m \rangle} \psi_m \tag{2.10}$$

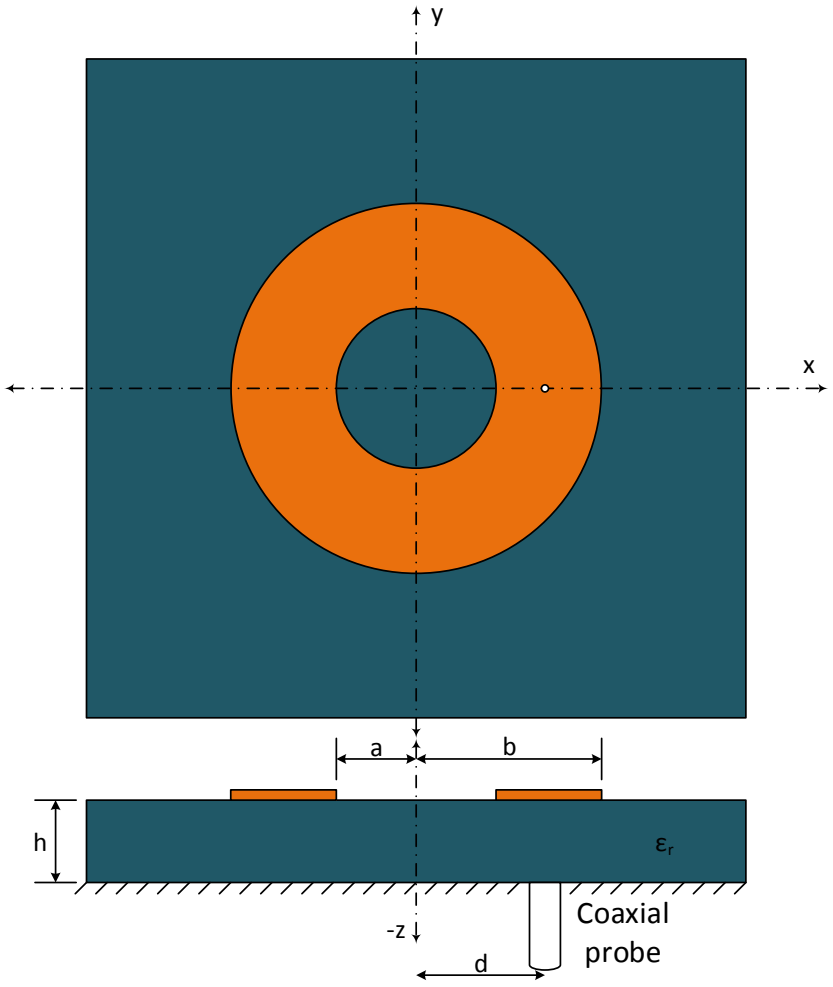

Fig. 4. Annular Ring patch geometry and design variables.

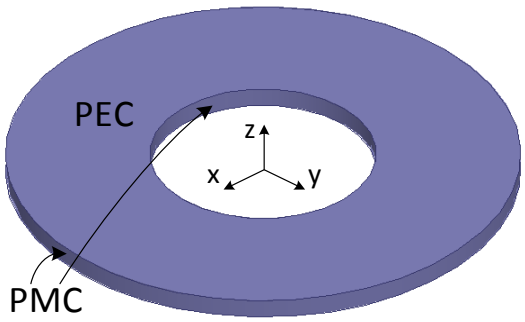

Fig. 5. Cavity model of Annular Ring patch showing PEC and PMC walls (ground plane not shown).

where $\langle J\psi_m \rangle = \int J\psi_m^* \, ds$ and $\langle \psi_m \psi_m \rangle = \int \psi_m \psi_m^* \, dv$. Available in [9] is a list of resonant mode equations and the one pertaining to the annular ring is given below:

$$\psi_{mn} = \left[\mathrm{N}_\mathrm{n}^{'}\left(k_{mn}a\right) \mathrm{J}_\mathrm{n}\left(k_{mn}\rho\right) - \mathrm{J}_\mathrm{n}^{'}\left(k_{mn}a\right) \mathrm{N}_\mathrm{n}\left(k_{mn}\rho\right) \right] e^{jn\phi} \tag{2.11}$$

The solution for (2.10) is provided in [8], for the resonant equation (2.11):

$$E_z = j\omega\mu_0 J \left(\sum_{m=1}^{\infty} \sum_{n=0}^{\infty} R_{mn} \left(\begin{matrix} \mathrm{N}_\mathrm{n}^{'}\left(k_{mn}a\right) \mathrm{J}_\mathrm{n}\left(k_{mn}\rho\right) - \\ \mathrm{J}_\mathrm{n}^{'}\left(k_{mn}a\right) \mathrm{N}_\mathrm{n}\left(k_{mn}\rho\right) \end{matrix} \right) \right) \cos n\varphi \tag{2.12}$$

where

$$R_{mn} = \begin{cases} \dfrac{k^2 \pi w \left(\mathrm{N}_0^{'}\left(k_{m0}\, a_{eff}\right) \mathrm{J}_0\left(k_{m0}\, d\right) - \mathrm{J}_0^{'}\left(k_{m0}\, a_{eff}\right) \mathrm{N}_0\left(k_{m0}\, d\right) \right)}{2\left(k_d^2 - k_{m0}^2\right) \left(\dfrac{\mathrm{J}_0^{'\,2}\left(k_{m0}\, a_{eff}\right)}{\mathrm{J}_0^{'\,2}\left(k_{m0}\, b_{eff}\right)} - 1 \right)} & , n = 0 \\ \dfrac{k^2 \pi \sin nw \cos n\pi \left(\mathrm{N}_\mathrm{n}^{'}\left(k_{mn}\, a_{eff}\right) \mathrm{J}_\mathrm{n}\left(k_{mn}\, d\right) - \mathrm{J}_\mathrm{n}^{'}\left(k_{mn}\, a_{eff}\right) \mathrm{N}_\mathrm{n}\left(k_{mn}\, d\right) \right)}{2\left(k_d^2 - k_{mn}^2\right) \left(\dfrac{\mathrm{J}_\mathrm{n}^{'\,2}\left(k_{mn}\, a_{eff}\right)}{\mathrm{J}_\mathrm{n}^{'\,2}\left(k_{mn}\, b_{eff}\right)} - 1 \right)} & , n \neq 0 \end{cases} \tag{2.13}$$

and $k_d = \omega\sqrt{\mu_0 \epsilon}$. This double summation can be solved for $m, n \leq 5$ as it is rapidly convergent [8].

This structure has fringing fields that exist at the interior and exterior PMC walls, and those fields encounter non-homogenous media, giving rise to an effective dielectric constant which is given by (2.6). Here, however, the width of the patch is given by:

$$W = (b - a) \tag{2.14}$$

Simplified forms of effective radii due to fringing fields are given by [8]:

$$\begin{aligned} a_{eff} &= a - \frac{3}{4}t \\ b_{eff} &= b + \frac{3}{4}t \end{aligned} \tag{2.15}$$

To obtain the radiation fields from (2.12), which are the fields inside the cavity, equivalent sources representing the fields on the PMC walls are determined. Following the same principle as in the rectangular patch, surface magnetic currents are accounted for, taking into account its image due to the ground plane, and the far-field electric field components are given by:

$$E_\theta = j^n \left(\frac{2tk_0 E_{0mn}}{\pi k_{mn}} \right) \left(\frac{e^{-jk_0 r}}{r} \right) \cos n\phi \left[\begin{array}{c} \mathrm{J}_\mathrm{n}^{'}(k_0 a_{eff} \sin\theta) - \\ \mathrm{J}_\mathrm{n}^{'}(k_0 b_{eff} \sin\theta) \dfrac{\mathrm{J}_\mathrm{n}^{'}(k_{mn} a_{eff})}{\mathrm{J}_\mathrm{n}^{'}(k_{mn} b_{eff})} \end{array} \right] \tag{2.16}$$

and

$$E_{\phi} = -j^{n}\left(\frac{2tnE_{0mn}}{\pi k_{mn}}\right)\left(\frac{e^{-jk_0 r}}{r}\right)\cot\theta\sin n\phi\left[\begin{array}{c}\dfrac{\mathrm{J_n}\left(k_0 a_{eff}\sin\theta\right)}{a} - \\ \dfrac{\mathrm{J_n}\left(k_0 b_{eff}\sin\theta\right)}{b}\dfrac{\mathrm{J_n}'\left(k_{mn}a_{eff}\right)}{\mathrm{J_n}'\left(k_{mn}b_{eff}\right)}\end{array}\right] \tag{2.17}$$

The input impedance varies along the width of the patch for different positions of the coaxial probe feed. It is determined by taking into account various losses in the cavity and surrounding region, such as radiation loss, dielectric loss, conductor loss and surface wave loss [8], [10]. The expression for the input impedance is given as follows:

$$\begin{aligned} Z &= R + jX \\ &= j\omega\mu t\sum_{m=1}^{\infty}\frac{\left(\mathrm{J_0}\left(k_{m0}d\right)\mathrm{N_0}'\left(k_{m0}a'\right) - \mathrm{J_0}'\left(k_{m0}a'\right)\mathrm{N_0}\left(k_{m0}d\right)\right)^2}{\dfrac{4\left(k_{eff}^2 - k_{m0}^2\right)}{\pi k_{m0}^2}\left(\dfrac{\mathrm{J_0}'^2\left(k_{m0}a'\right)}{\mathrm{J_0}'^2\left(k_{m0}b'\right)} - 1\right)} + \\ &\sum_{m=1}^{\infty}\sum_{n=1}^{\infty}\frac{\dfrac{\sin^2 nw}{nw}\left(\mathrm{J_n}\left(k_{mn}d\right)\mathrm{N_n}'\left(k_{mn}a'\right) - \mathrm{J_n}'\left(k_{mn}a'\right)\mathrm{N_n}\left(k_{mn}d\right)\right)^2}{\dfrac{2\left(k_{eff}^2 - k_{m0}^2\right)}{\pi k_{m0}^2}\left(\dfrac{\mathrm{J_0}'\left(k_{mn}a'\right)}{\mathrm{J_0}'\left(k_{mn}b'\right)}\left(1 - \dfrac{n^2}{k_{mn}^2 b'^2}\right) - \left(1 - \dfrac{n^2}{k_{mn}^2 a'^2}\right)\right)} \end{aligned} \tag{2.18}$$

where

$$\begin{aligned} k_{eff} &= k_0\sqrt{\epsilon_{eff}\left(1 - j\delta_{eff}\right)} \\ \delta_{eff} &= \tan\delta + \frac{1}{t\sqrt{\sigma\mu\pi f}} + \frac{2\omega\mu t I}{\eta_0\epsilon_r\left(\dfrac{\mathrm{J_0}'\left(k_{mn}a'\right)}{\mathrm{J_0}'\left(k_{mn}b'\right)}\left(1 - \dfrac{n^2}{k_{mn}^2 b'^2}\right) - \left(1 - \dfrac{n^2}{k_{mn}^2 a'^2}\right)\right)} \end{aligned} \tag{2.19}$$

Here, δ_{eff} is the effective loss tangent; $\tan\delta$ is the loss tangent of the substrate; σ is conductivity of patch and ground plane; η_0 is characteristic impedance of free space; and I is given by:

$$I = \int_0^{\pi} \frac{n^2 \cos^2\theta}{k_0^2 \sin\theta} \left\{ \frac{\mathrm{J_n}\left(k_0 a' \sin\theta\right)}{a'} - \frac{\mathrm{J_n}\left(k_0 b' \sin\theta\right)}{b'} \frac{\mathrm{J_n'}^2\left(k_{mn} a'\right)}{\mathrm{J_n'}^2\left(k_{mn} b'\right)} \right\}^2 + \sin\theta \left\{ \mathrm{J_n'}\left(k_0 a' \sin\theta\right) - \mathrm{J_n'}\left(k_0 b' \sin\theta\right) \frac{\mathrm{J_0'}^2\left(k_{mn} a'\right)}{\mathrm{J_0'}^2\left(k_{mn} b'\right)} \right\} d\theta \tag{2.20}$$

Equation (2.18) could be used to plot the impedances across a band of frequencies or along the width of the patch. The former allows for a better tuning of the resonant radii, while the latter allows for an optimum placement of the coaxial probe feed in order to achieve the required amount of input impedance. As the case of (2.12), (2.18) is also rapid convergent, and it is sufficient to include terms up to $m, n \leq 5$ [8].

2.4 Yagi-Uda Antenna Array

This antenna traditionally comprises a linear array of dipole antenna of which one is excited, while the others behave as parasitic radiators. Fig. 6 depicts a Yagi-Uda array of linear elements. The driven element, being a dipole, has an omnidirectional radiation pattern, with nulls in the broadside direction (z-axis). However, in the presence of these parasitic elements, the radiator behaves as an end-fire array, and the main beam is directed towards the positive y-axis. The parasitic elements to the right of the driven element, from Fig. 6, act as directors while those to the left act as reflectors [7]. Due to

its end-fire beam formation in the direction of the directors, the gain achieved is much higher than that of the driven element.

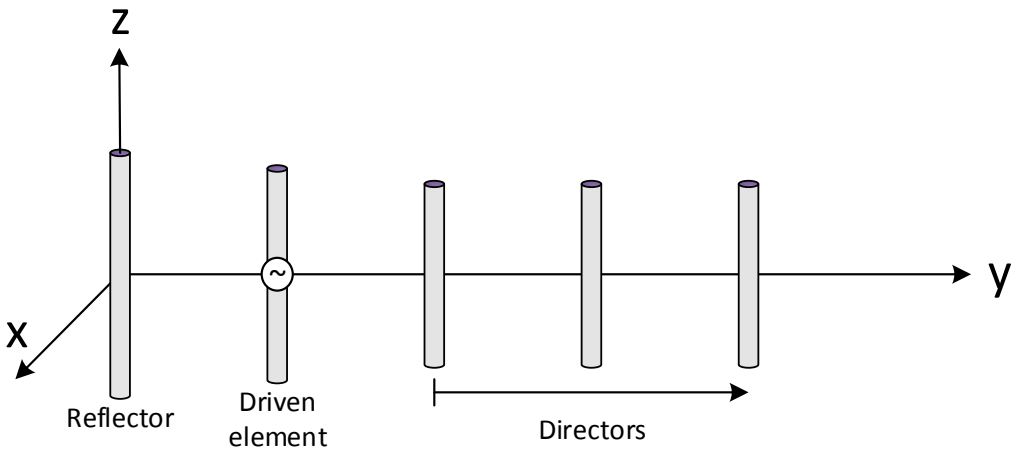

Fig. 6. Yagi-Uda Linear Antenna Array Configuration.

To achieve this end-fire beam, as explained in [7], the directors are designed to be smaller than the driven element. If the driven element is typically a half wavelength dipole (with a length of $0.45-0.49\lambda$), the directors are about $0.40-0.45\lambda$ long. All the directors need not be of the same length for optimum design, and may vary depending on the application and desired results, but for the purpose of this thesis, the number of directors is limited to one. The reflector on the other hand is slightly longer than the driven element, typically larger than 0.50λ. The spacing between the directors as well as that between the driven element and the first director plays a major role in the gain of the Yagi-Uda array. It was experimentally shown that for spacing greater than 0.30λ, there was a significant drop in the gain of the array. However, the gain was more-or-less

independent of spacing for up to approximately 0.30λ [7]. An optimum spacing between the driven element and the reflector was calculated to be around 0.25λ.

2.5 RF Diodes

To achieve reconfiguration mechanisms in this antenna, RF PIN diodes and varactor diodes are utilized. These devices are non-linear solid-state semiconductor devices, wherein with a certain amount of bias voltage, the I-V characteristics are altered. In the case of a varactor diode though, reverse bias voltage gives rise to a series capacitance, and this voltage can be further tuned to obtain desired results.

These devices operate on similar principles as a PN junction diode, where a semiconductor doped with negatively charged atoms, creating excess amounts of holes, denote a P-type, while positively charged atoms, creating an excess amount of electrons, denote an N-type semiconductor [3]. A PN junction is formed when the P and N type semiconductors are joined, and near this junction, diffusion of holes and electrons creates a depletion region (a region with no charge carriers) as the electrons and holes combine to cancel any excessive charge. This lack of charge carriers causes an electric field across the junction, arising due to the positive and negative charges in the N and P type regions. This in turn gives rise to a potential barrier across the junction, causing holes in the P-type and electrons in the N-type regions to move away from the junction and reducing current flow. Fig. 7 illustrates the depletion region formed.

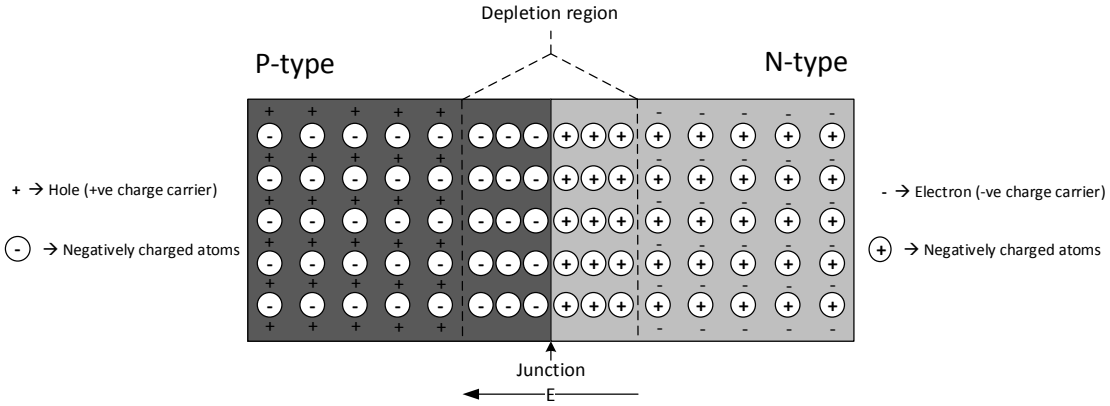

Fig. 7. PN junction diode is formed by fusing P-type and N-type semiconductors. Depletion region formed around the junction giving rise to an electric field.

An external voltage applied to the PN diode is known as bias voltage. Forward bias is when the P-type terminal has higher external potential than the N-type terminal and reverse bias is when the N-type terminal has higher external potential than the P-type terminal. Under forward bias conditions, holes on the P-type terminal are pushed toward the junction and similarly, electrons on the N-type terminal are pushed toward the junction. Due to this, the width of the depletion region decreases as there are more electrons and holes available near the junction, thus lowering the potential barrier; and beyond a threshold potential difference, electrons and holes drift across the junction. On the other hand, applying a reverse bias induces an opposite effect, wherein the depletion region widens due to attraction of holes and electrons at the P-type and N-type terminals respectively.

Due to the opposite behaviors under different biases, diodes can act as switches – forward bias resembles short circuit and reverse bias resembles open circuit. This holds good for DC and low frequencies. As the frequency increases and the diode switches

from “on” to “off” rapidly, the amount of time available for the stored charge in the depletion region to deplete in the “off” state may be lesser than the negative half cycle of the RF signal, and thus behaves as an open-circuit (rectifying the RF signal which increases distortion). This recovery time is termed as “reverse recovery time” and is a standard measure of a diode’s performance.

To overcome this effect and increase the reverse recovery time at RF frequencies, an un-doped semiconductor layer (also known as an intrinsic layer) is placed at the PN junction. This layer stores charge and thus increases the amount of charge carriers flowing through the junction between the P-type and N-type regions, when forward biased. This increases the reverse recovery time and the diode would still behave as a short circuit for the negative half cycle of the signal.

RF varactor diodes are a source of solid-state variable capacitors when the diodes are reverse biased. As mentioned earlier, when the diode is reverse biased, the depletion region widens and increases the potential barrier. This gives rise to a junction capacitance which varies as the magnitude of the reverse bias voltage is varied. With respect to RF designs, it allows the designer to vary capacitance between two terminals thus making a transmission line look electrically longer or shorter without physically modifying the transmission line.

CHAPTER III

DESIGN OF A POLARIZATION RECONFIGURABLE BROADBAND ANNULAR RING PATCH ANTENNA

This chapter describes the process involved in the design of an antenna with an impedance bandwidth of at least 100MHz centered around 2.45GHz (~4% fractional bandwidth).

3.1 Single Layer Annular Ring Patch (ARMSP) Antenna

The first iteration of the design started with the study of the cavity model of annular ring patch antennas as described in section 2.3. To validate the model and thus use it for the intended design, analysis was performed using MATLAB (analytical solutions) and HFSS (full-wave CAD simulations) and compared with results presented in [8]. With the antenna dimensions $a = 35mm$, $b = 70mm$, $d = 37mm$, $\epsilon_r = 2.32$ and $t = 1.59mm$. Table 1 summarizes the resonant frequencies obtained across analytical solutions, HFSS simulations, calculated and measured data. The analytical values were obtained from (2.7) and (2.8). Fig. 8 shows the analytical and simulated values for input impedance of the patch at TM_{11} mode where analytical solutions were obtained from (2.18). The agreement between the analytical and simulated data is good, except that the peaks of the impedances are slightly off. This could be attributed to having a finite ground plane in the simulated measurements, the model of the coaxial connector to the

annular ring patch or differences in the dielectric losses and metal conductivity between the analytical and simulated versions, which could shift the frequency of resonance.

Table 1. Comparison of analytical and CAD simulations against calculated and measured data presented in [8].

Mode (TM_{mn})	Measured [8] (MHz)	Calculated [8] (MHz)	Analytical (MHz)	HFSS (MHz)
TM_{11}	625	618	623	614
TM_{12}	1230	1220	1228	1214
TM_{13}	1800	1790	1805	1792
TM_{14}	–	2335	2351	2344
TM_{21}	2760	2820	2839	2870
TM_{22}	3037	3068	3089	2975
TM_{23}	3446	3450	3475	3378
TM_{24}	3940	3935	3962	3870

Having established that there is a close agreement between the cavity model and a full-wave simulation model and that these model also agree with the data presented in [8], the model parameters were modified to find an optimum geometry for a TM_{11} mode annular ring patch antenna with a resonance at 2.45 GHz.

At 2.45 GHz, the corresponding wave number was calculated using (2.7). To then find out the patch dimensions using (2.8), it was fixed that the outer radius of the annular ring was twice that of the inner. The substrate chosen was Rogers RT/duroid

5880 with the following substrate parameters: $\epsilon_r = 2.2$, $t = 1.5748mm$ and $\tan\delta = 0.0009$. The reason for a low dielectric substrate is that it has a relatively low loss tangent and therefore lesser dielectric losses. With these parameters, the analytically computed radii were $a = 11mm$ and $b = 22mm$. These values gave a resonant peak at approximately 2.1 GHz. After further optimization to shift the resonant peak to the desired frequency, the radii obtained were $a = 9mm$ and $b = 20mm$. Fig. 9 shows the input impedance obtained from the HFSS simulated model for the initial and the final configuration.

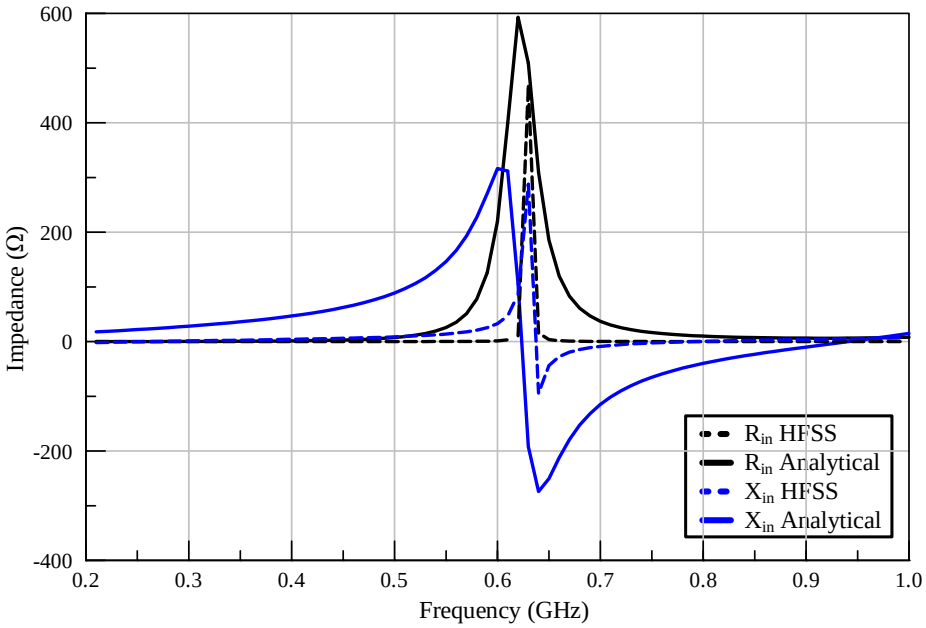

Fig. 8. Analytical and simulated input impedances of TM_{11} mode of annular ring patch antenna.

The reflection coefficient of the optimized configuration of the single layer ARMSP antenna is presented in Fig. 10. It is clearly evident that there is a poor

impedance match to a 50Ω input coaxial line. Further simulations found no probe positions along the width of the ARMSP with minimal reflections. If the coaxial probe feed impedance is shifted to 550Ω (the actual impedance of the patch, obtained from Fig. 9), the reflections are drastically reduced (also shown in Fig. 10). This solution is, however, impractical as the standard for RF systems is 50Ω and was only examined to measure the impedance bandwidth of the antenna $(\approx 0.9\%)$.

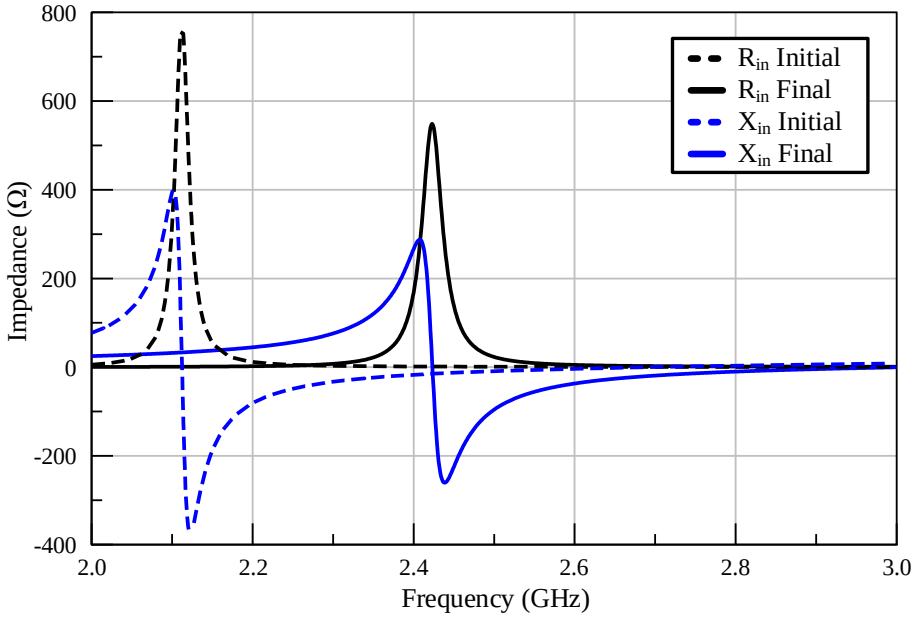

Fig. 9. Input impedance of simulated single layer ARMSP antenna showing initial design (a=11mm, b=22mm) vs. optimized design (a=9mm, b=20mm).

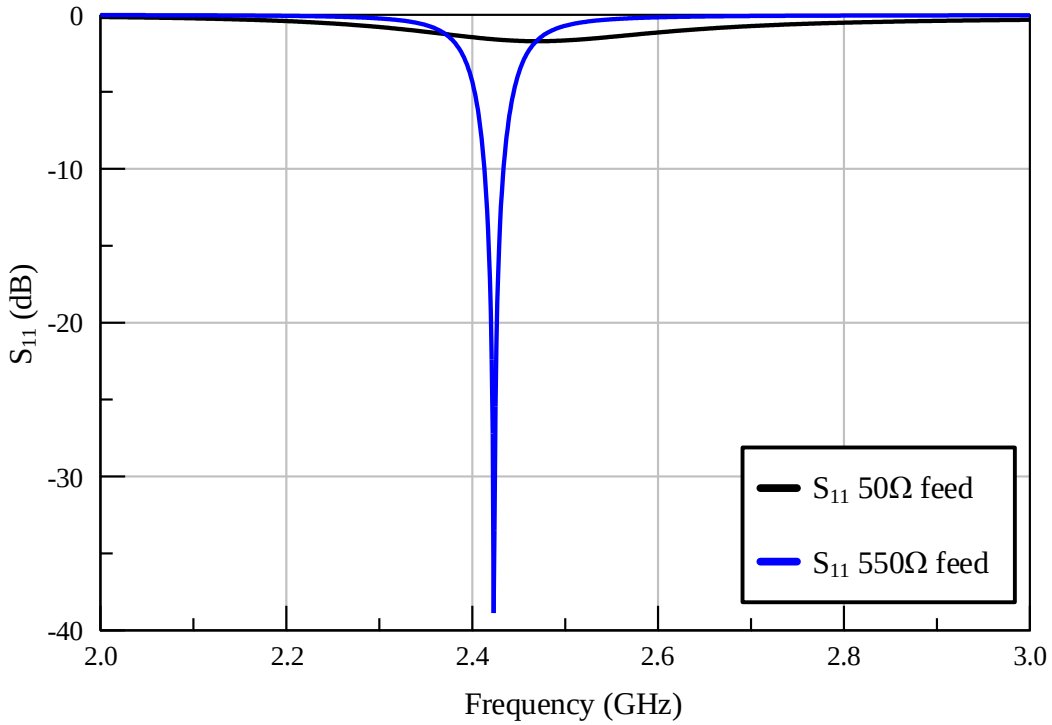

Fig. 10. Reflection coefficient of single layer ARMSP antenna – comparison between 50Ω and 550Ω coaxial feed line. Impedance bandwidth ≈0.9%.

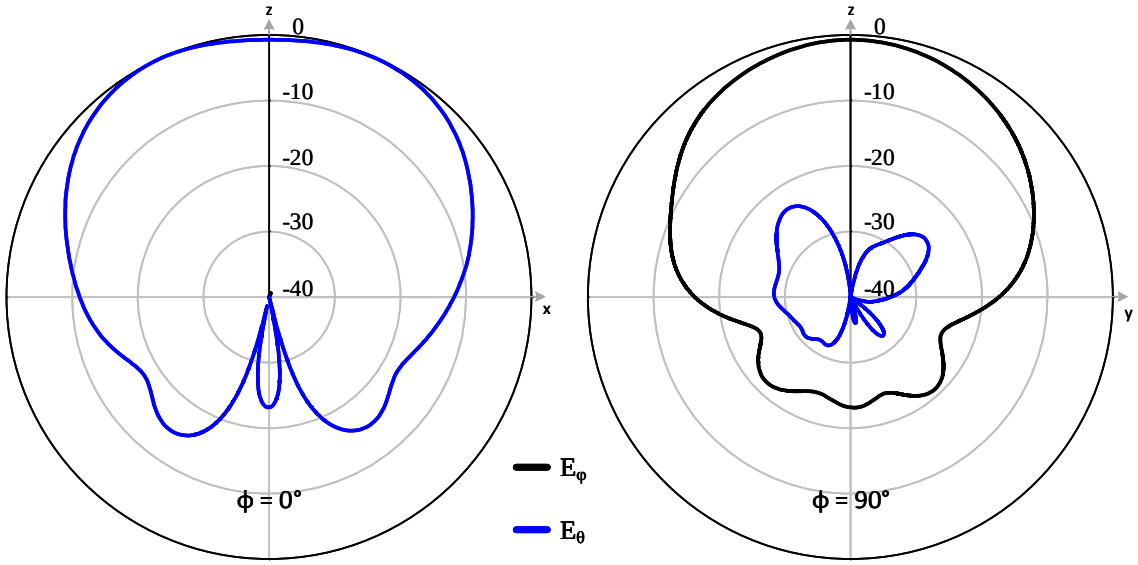

Fig. 11. Normalized radiation pattern of single layer ARMSP antenna at 2.45 GHz.

3.2 Stacked ARMSP Antenna

As calculated earlier, it was obtained that the impedance bandwidth of the ARMSP antenna was approximately 0.9%, which is far less than what is required. To tackle this issue, a concept of stacked patch was studied and simulated. From [11] it was understood that having a lower dielectric constant substrate as the first layer along with a layer of foam above it allows for a wider impedance bandwidth, as compared to having a larger dielectric constant first substrate. It is also stated that the lower radiating patch must be strongly capacitive in order for the stacked patch as a whole to be better impedance matched. From Fig. 9, we can say that at frequencies near 2.45 GHz, the patch is strongly capacitive and behaves as a good starting point for a stacked design with no further alterations required.

The second substrate was fixed to be a Rogers RT/duroid 5880 substrate with half the thickness ($t_3 = 0.787mm$) as the bottom one. These two substrates are separated by a foam of thickness t_3, with dielectric constant $\epsilon_r = 1.06$ and $\tan\delta = 0.0001$. The second layer patch was designed as a 2.45 GHz resonant ARMSP antenna but with varying dielectric constants and overall thickness of the effective substrate accounted for. As suggested in [11], a starting point for the foam thickness could be approximately $0.06\lambda_g$, which was roughly $6mm$ thick. Fig. 12 illustrates the 3D model of the stacked patch.

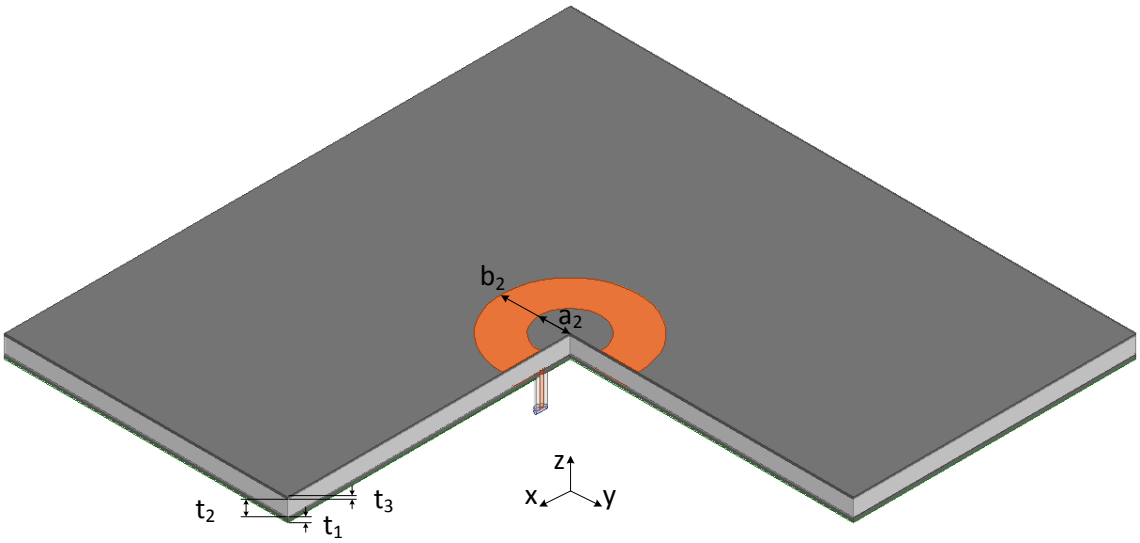

Fig. 12. HFSS 3D model cut-out of the stacked ARMSP antenna; a_2 and b_2 are the inner and outer radii, respectively, of the stacked patch element, t_1, t_2 and t_3 denote the thickness of the first layer substrate, foam and second layer substrate, respectively.

Keeping the foam thickness fixed, the values of a_2 and b_2 were optimized and eventually set to be $a = 11mm$ and $b = 24mm$. With this configuration, a much larger impedance bandwidth was achieved and as shown in [11], a resonant loop was observed in the Smith chart. Now, keeping the second layer patch radii fixed, the foam thickness t_2 was varied. It was observed that as the foam thickness was reduced, the resonant loop in the Smith chart became larger. In the initial case (where $t_2 = 6mm$), from Fig. 13, it can be observed that the resonant loop does not surround the center of the chart, and hence a narrower impedance bandwidth is noticed. With the foam thickness $t_2 = 5.5mm$, however, it is observed that the loop is formed around the center and a wider impedance bandwidth is achieved.

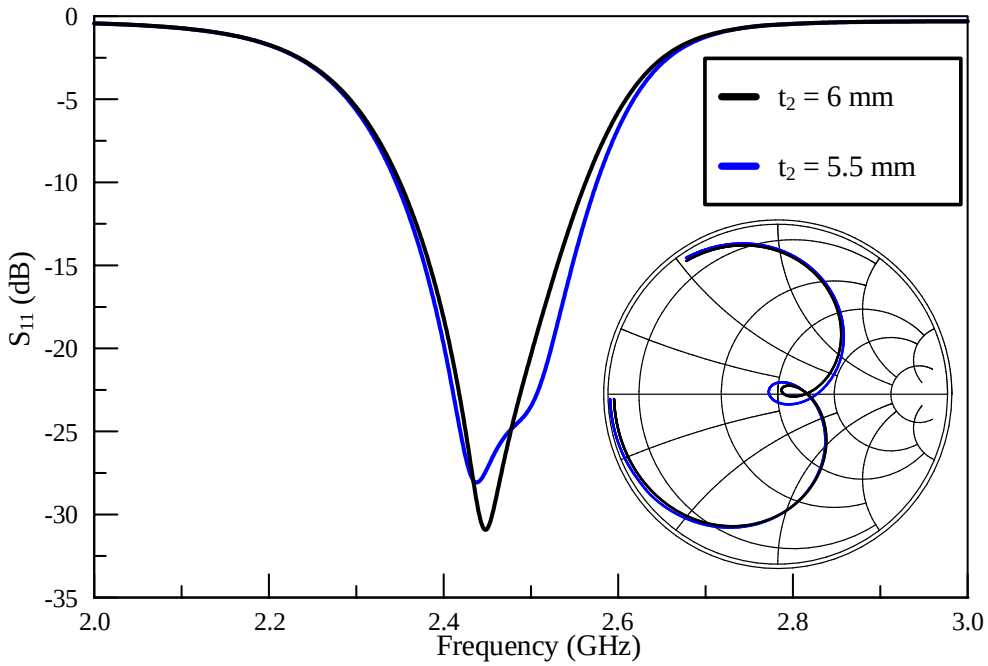

Fig. 13. Effect of varying foam thicknesses on the reflection coefficient and impedance bandwidth of a stacked ARMSP antenna.

With $t_2 = 6mm$, an impedance bandwidth of 8.7% was observed and with $t_2 = 5.5mm$, an impedance bandwidth of 9.3% was observed, both of which were more than twice the bandwidth desired. The simulated radiation pattern for the stacked configuration with $t_2 = 5.5mm$ is presented in Fig. 14.

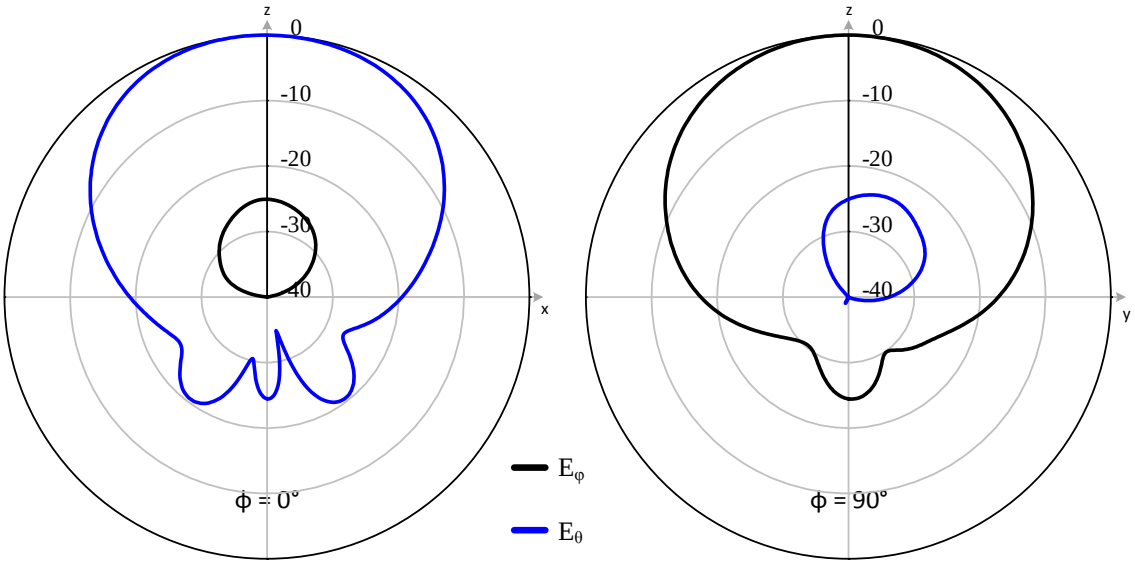

Fig. 14. Normalized radiation pattern for a stacked ARMSP antenna with $t_2 = 5.5mm$, at 2.45 GHz.

3.3 Polarization Reconfiguration on Stacked ARMSP Antenna

Now that a broadband behavior is achieved in the radiating element, a polarization reconfiguration mechanism is introduced. The types of polarization expected are linear and circular polarizations. Each of these has two orthogonal types, viz., horizontal and vertical linear polarizations as well as left-hand and right-hand circular polarizations. To achieve all four types of polarizations on one radiating element, the most straightforward approach is to have dual feeds on the antenna. The antenna presented in sections 3.1 and 3.2 are designed to operate at 2.45 GHz with the dominant mode (TM_{11}). When the dominant mode is excited, the surface currents on the patch are either vertically or horizontally oriented. This behavior aids in the placement of second feed port. Due to the innate orthogonality along the two axes on the surface of

the patch in the TM_{11} mode, the two feed ports can be placed at right angles to each other. So if either of one is excited, either vertical or horizontal polarization is achieved. This is illustrated with the help of Fig. 15.

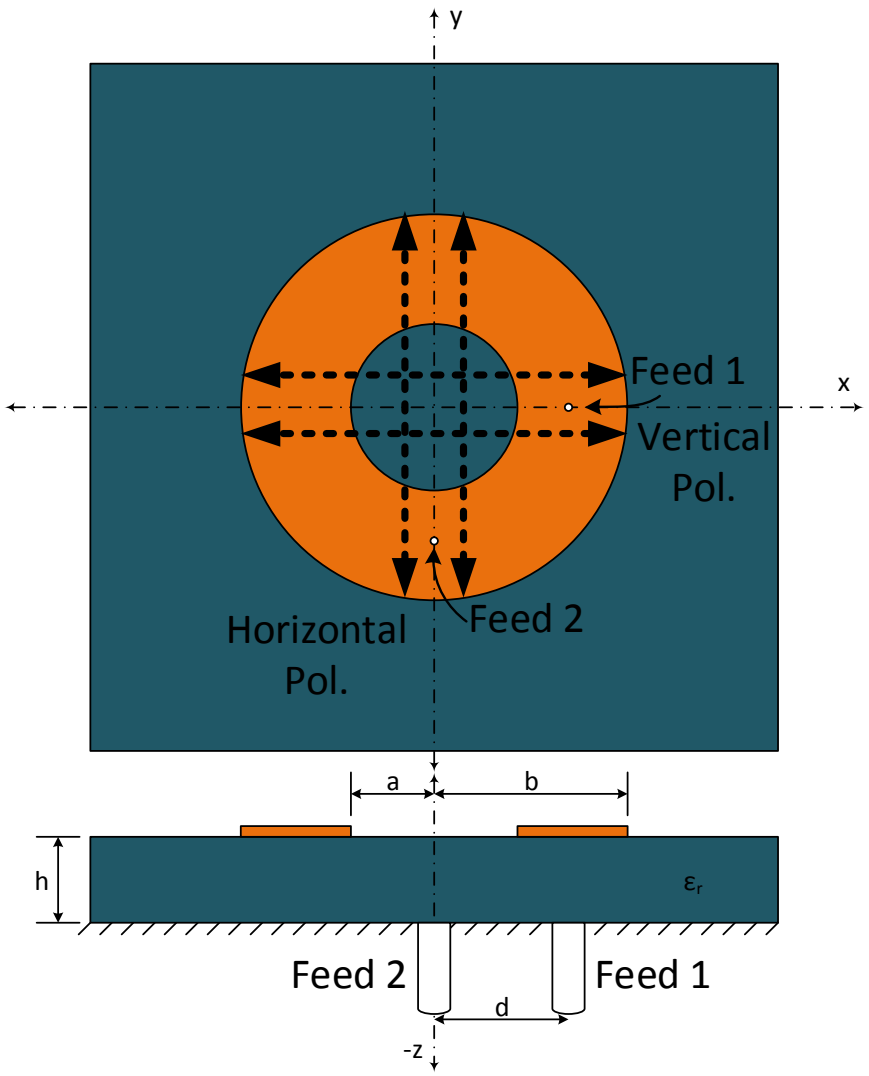

Fig. 15. Illustration of a dual feed ARMSP giving rise to horizontal and vertical linear polarizations in TM_{11} mode. Vertical polarization is observed along the xz-plane and horizontal polarization, along the yz-plane.

In [7], it is stated that circular polarization can be achieved in a dual feed antenna if the feeds are right angles to each other (if the antenna is designed to excite the dominant mode) and if the phase difference between the feeds are 90° (leading or lagging). Depending on the sign of the relative phase difference between the feed ports, the polarization achieved is either right-hand or left-hand circularly polarized.

Fig. 16 presents the complete S-parameters of the dual feed stacked ARMSP antenna. It is evident that both S_{11} and S_{22} are almost identical and well matched to their respective feed ports. There is also a strong isolation between the two ports, which is represented by S_{21}.

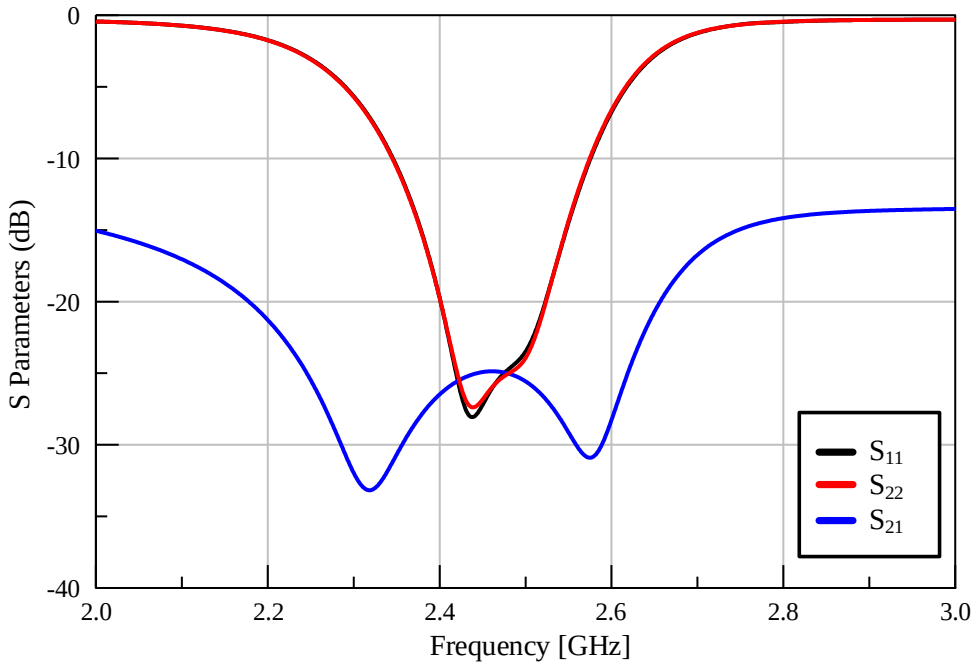

Fig. 16. S-parameters of the dual feed stacked ARMSP antenna; both ports are matched across the desired bandwidth and there is high isolation between them.

Fig. 17 presents the simulated radiation patterns showing both the vertical and horizontal linear polarizations on the two primary cut-planes. Fig. 18 presents the simulated radiation patterns showing left-hand and right-hand circular polarizations on the two primary cut-planes. From both these figures, it is observed that the cross-polarization levels for each cut-planes are about 25dB lesser in magnitude than the co-polarization levels. This shows high orthogonality between the co- and cross-polarization fields.

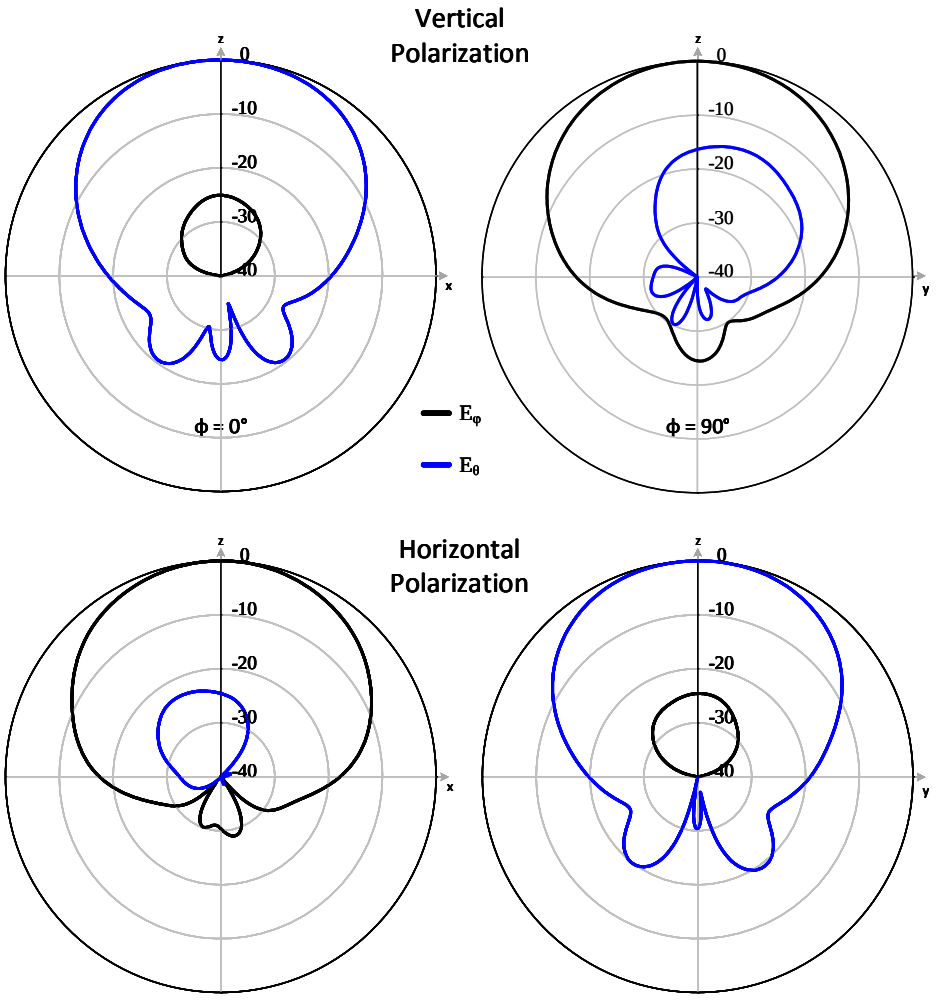

Fig. 17. Normalized radiation patterns for vertical and horizontal linear polarizations of stacked ARMSP antenna.

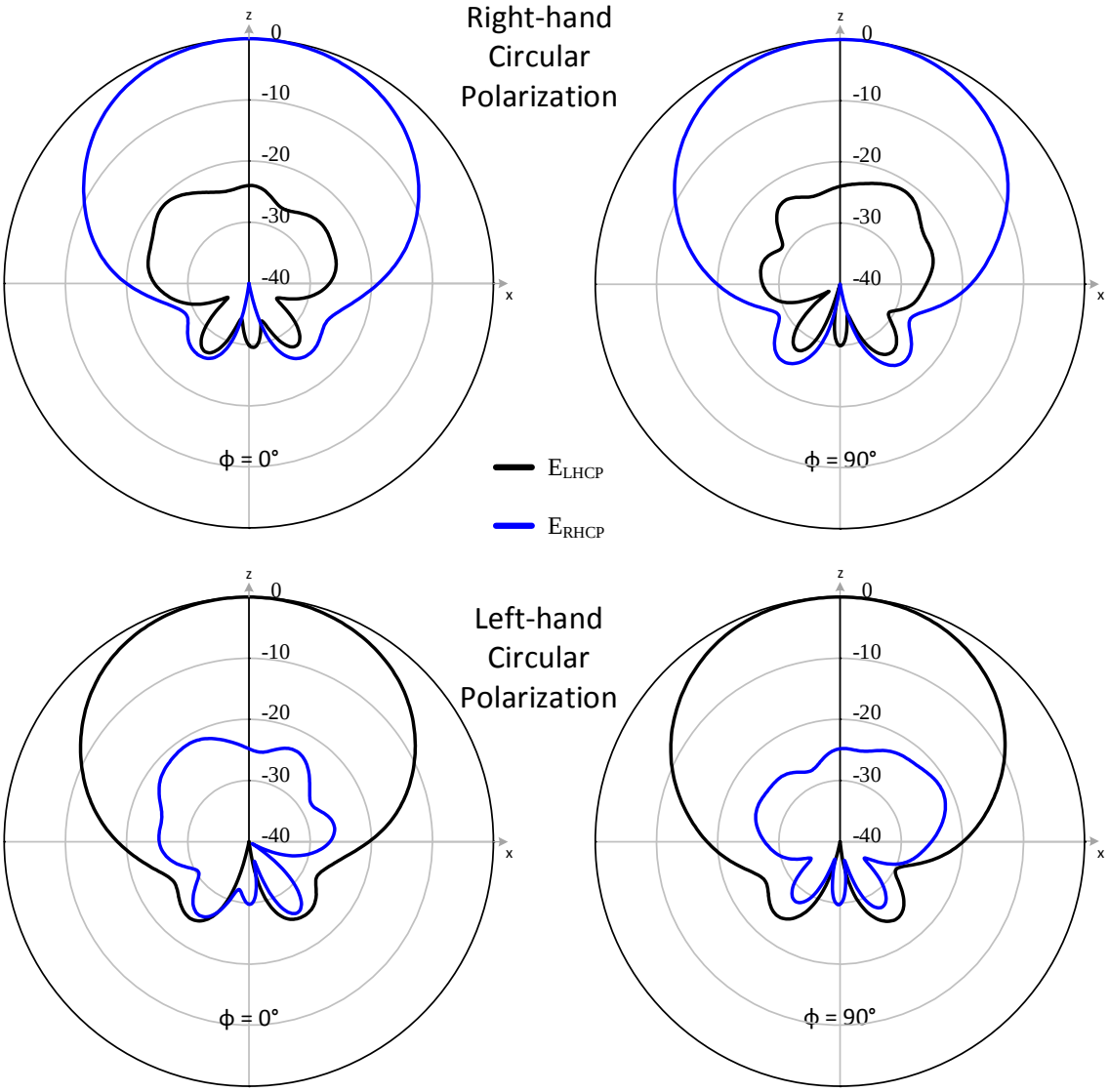

Fig. 18. Normalized radiation patterns showing right-hand and left-hand circular polarizations.

3.4 Polarization Reconfigurable Stacked ARMSP Antenna on Duroid 5870 Substrate

At this point, the substrate Rogers RT/duroid 5880 was unavailable for fabrication, so, its nearest alternative, Rogers RT/duroid 5870 (with a dielectric constant

$\epsilon_r = 2.33$ and $\tan\delta = 0.0009$) was chosen. Design parameters using the cavity model approach were used to start the initial simulation with the new substrate. This new design was then iteratively simulated and optimized on HFSS, starting with a single layer and then the stacked patch. During the design of the second ARMSP layer, the foam thickness was kept fixed and only the inner and outer radii were optimized. After finalizing the radii, the foam thickness was varied. The final optimized design parameters are presented in Table 2.

Table 2. Optimized design parameters for Stacked ARMSP Antenna on Duroid 5870 substrate.

Design Parameter	Value
Substrate-1 thickness (t_1)	1.5748 mm
Foam thickness (t_2)	4.5 mm
Substrate-2 thickness (t_3)	1.5748 mm
ARMSP-1 inner radius (a_1)	7.5 mm
ARMSP-1 outer radius (b_1)	20.5 mm
ARMSP-2 inner radius (a_2)	10 mm
ARMSP-2 outer radius (b_2)	23 mm
Probe feed location (from origin)	12 mm

Fig. 19 presents the port terminal parameters for this modified antenna, highlighting the broader bandwidth, minimal reflection on feed ports and high isolation

between the ports. The achieved impedance bandwidth is approximately 11%. The radiation patterns are almost identical to that of the previous design.

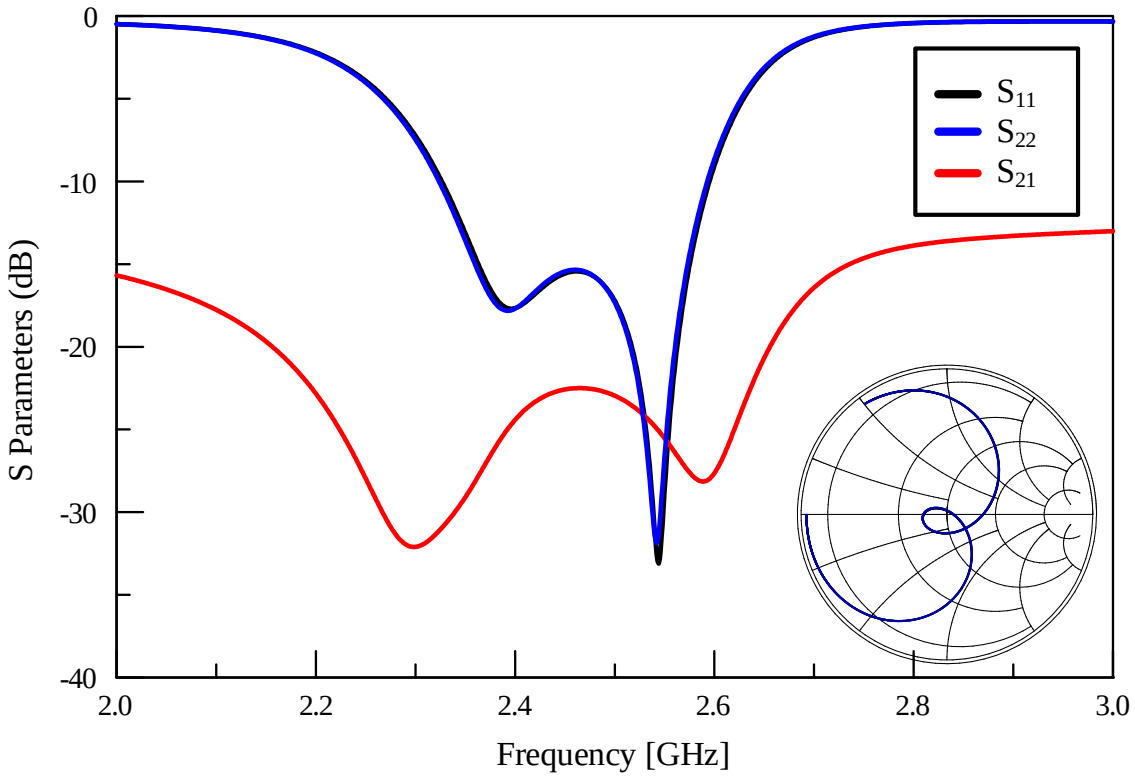

Fig. 19. S-parameters of the dual feed stacked ARMSP antenna with Duroid 5870 substrates. The impedance bandwidth achieved is approximately 11%.

CHAPTER IV

DESIGN OF A PATTERN RECONFIGURABLE BROADBAND ANNULAR RING PATCH ANTENNA

This chapter further develops the antenna from section 3.3 to enable steering of the main-beam for different polarizations, and thus, to achieve a basic form of pattern reconfiguration. It was mentioned in section 3.3 that due to substrate unavailability, the design had to be modified from duroid 5880 to duroid 5870. This was, however, executed after several design iterations of pattern reconfiguration mechanisms on duroid 5880 substrates (presented in sections 4.1 through 4.3); the design procedures remain the same, with only the physical dimensions having to be altered.

4.1 Quasi-Yagi Coupled Stacked ARMSP Antenna

The antenna presented in this section builds upon the parasitic array described in [4] and [5].

4.1.1 Effect of a Director on the Stacked ARMSP Antenna

The first iteration of adding the Yagi steering elements involved placing one microstrip element (director) on the same plane as the stacked ARMSP element. The length was designed for approximately $0.4\lambda_g$, width was designed to be approximately the same width as a 50Ω microstrip line. Fig. 20 illustrates this design. This director is intended to steer the beam when the antenna is fed in the second port (long the y-axis),

as the length of director is along the y-axis and is y-polarized. The port reflection parameters are presented in Fig. 21 and the radiation pattern is presented in Fig. 22.

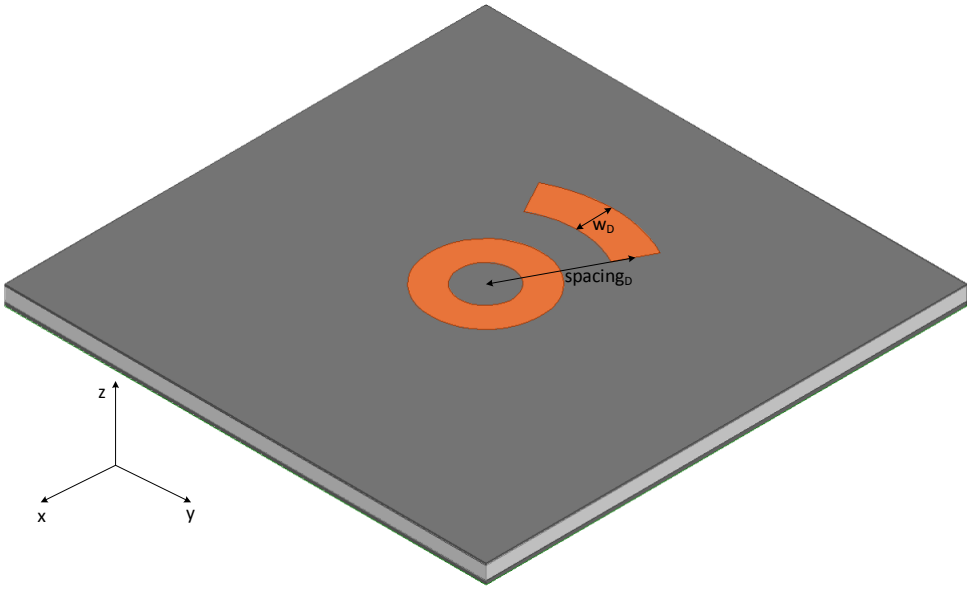

Fig. 20. Stacked ARMSP antenna with parasitic element (director) for beam-steering; w_D is the width of the director and $spacing_D$ is the spacing of the director from the center of the second layer ARMSP.

From Fig. 21, it is observed that when the antenna couples with a parasitic element, it makes the antenna largely capacitive, and since the director is shorter than a half-wavelength, the resonant frequency is shifted slightly higher. This director not only affects port 2, but also port 1, however the resonant frequency is not adversely affected.

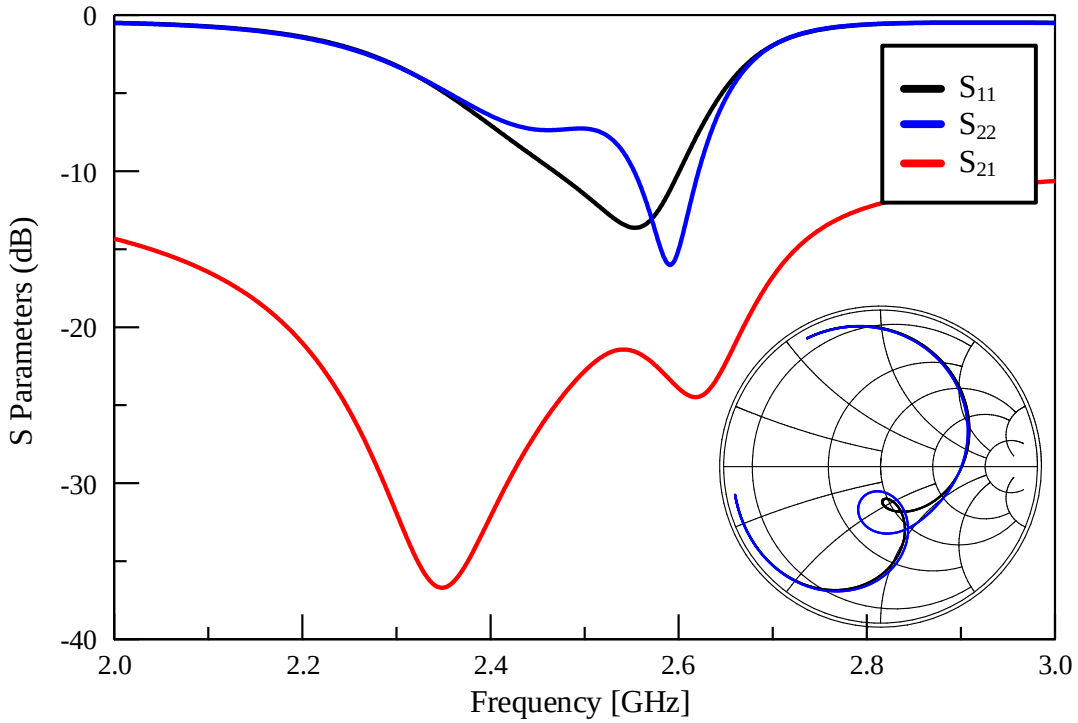

Fig. 21. Port reflection parameters for $w_D = 16mm$ and $spacing_D = 46mm$.

Fig. 22 shows the radiation pattern of this antenna. A beam tilt is observed in the horizontal polarization, which is due to the presence of the director. It can also be noted that the presence of a director along the negative x-axis does not affect the radiation properties of the vertical polarization configuration. In order to obtain beam-steering for vertical polarization, the director must be placed along the y-axis, and port 1 must be energized to couple with it.

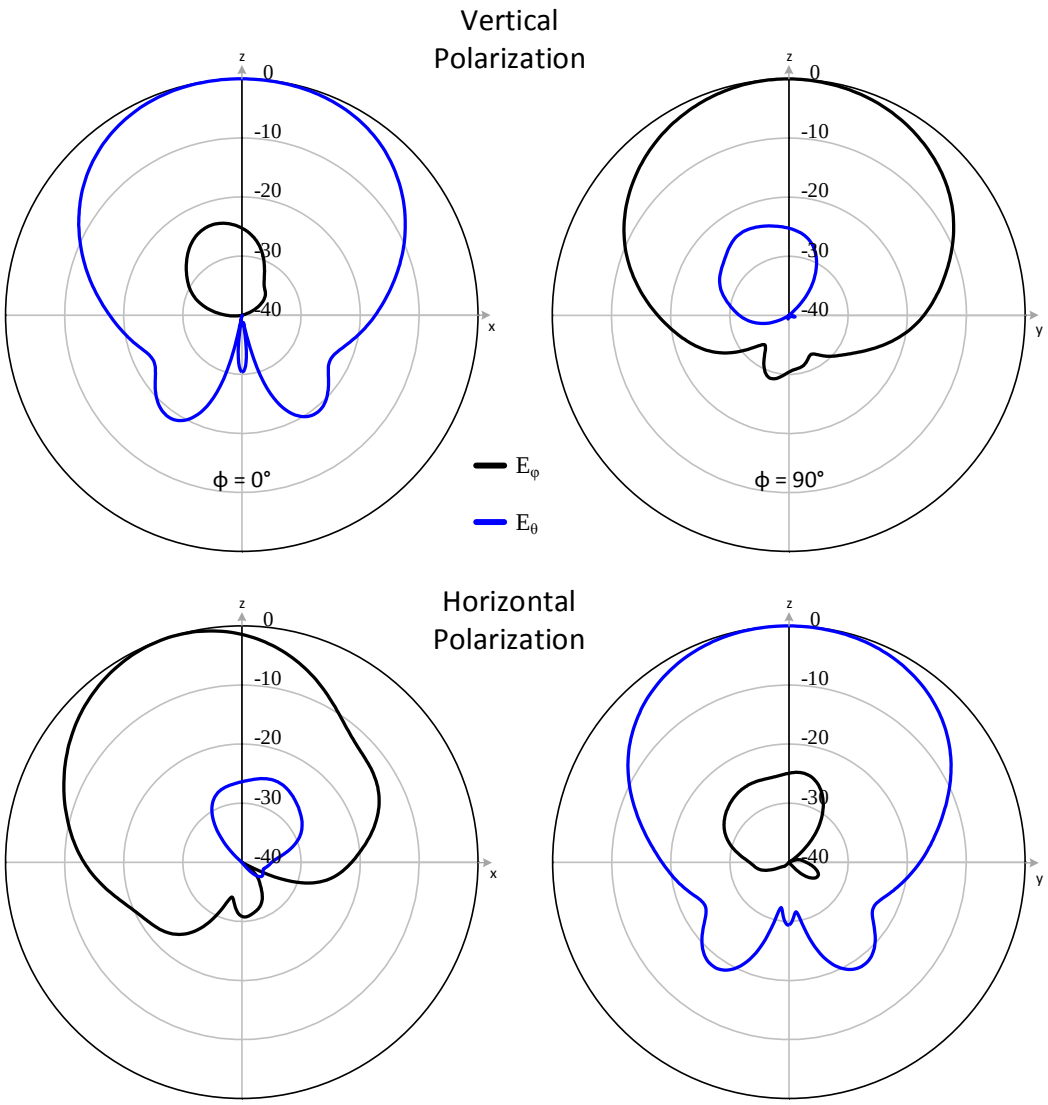

Fig. 22. Normalized radiation patterns showing about 20° of beam tilt towards negative axis. The patterns along vertical polarization plane remains unaltered.

The configuration presented so far serves as a good starting point to further investigate the effects of adding parasitic elements, their dimensions and their positions.

4.1.2 Effect of Adding a Foam Layer between the Stacked ARMSP and Yagi-Elements

From the previous design, it was observed that there was a strong coupling between the director and the antenna, giving rise to a large capacitance. In order to reduce the amount of coupling, a layer of low dielectric foam (thickness $t_4 = 7mm$) was introduced to add a physical separation between the antenna and the Yagi-elements. To also make the Yagi-elements layer easily manufacturable, they were simulated atop a duroid 5880 substrate (thickness $t_5 = 0.787mm$).

With this configuration, it was observed that while the antenna still maintained the beam tilt of about $20°$, the excessive capacitance issue was solved. There were, however, large reflections observed. In order to improve the port reflections, the foam thickness t_2 (between the two ARMSP elements) was varied. The results are presented in Fig. 23.

4.1.3 Effect of Introducing Reflector Element

Having been able to have an acceptable port impedance match with some amount of beam tilt, a reflector element was added at the same spacing and as the same width as the director but with a length approximately $0.5\lambda_g$. This however did not aid in a larger beam-tilt and the port reflection parameters were similar to that obtained in Fig. 23 for $t_2 = 3.5mm$.

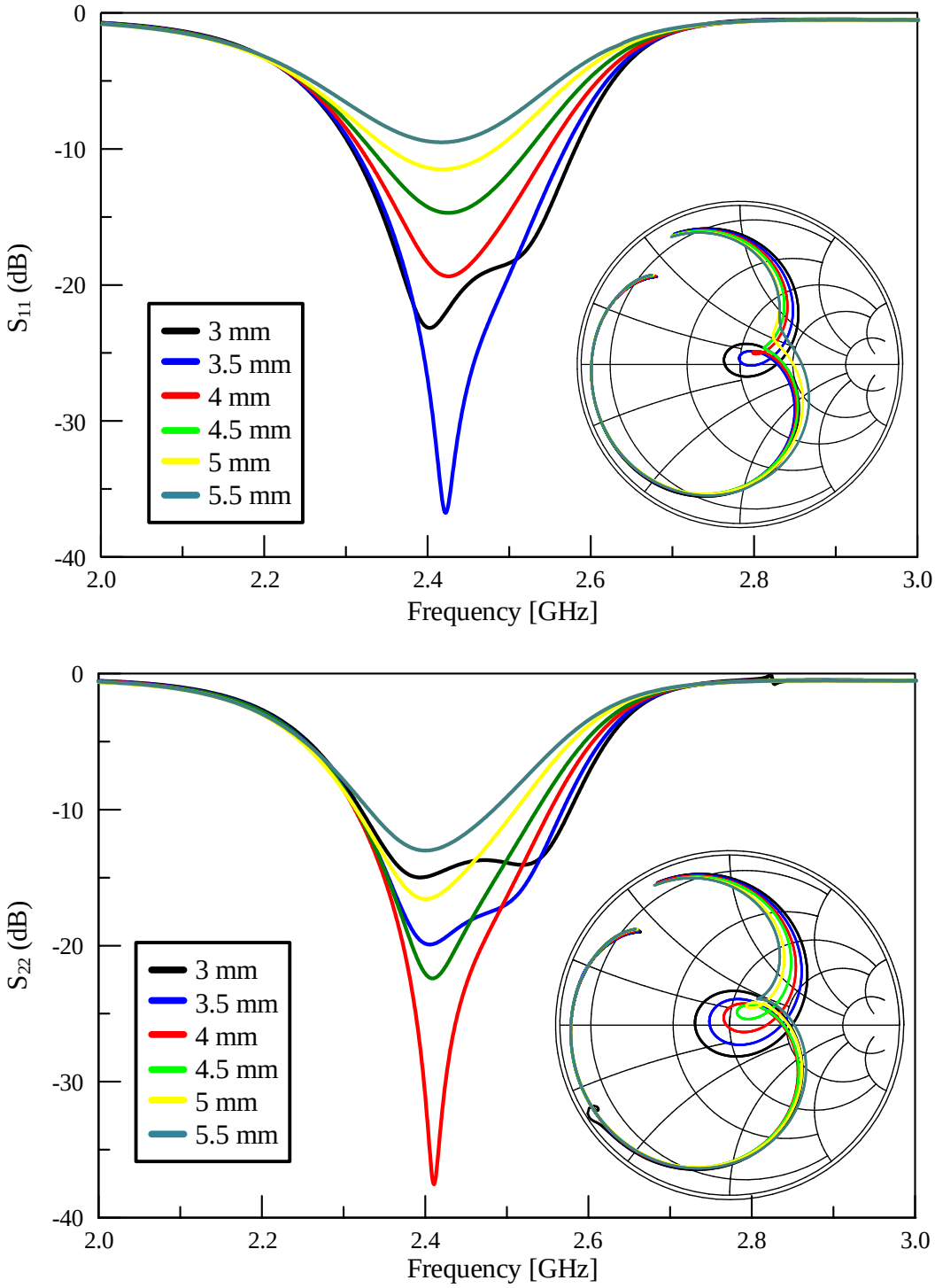

Fig. 23. Port reflection parameters for different values of foam thicknesses ($t_2 = 3mm\ to\ 5.5mm$). The final value chosen at this stage was $t_2 = 3.5mm$.

4.1.4 Effect of Increasing Foam Thickness (t_4) between Stacked ARMSP Antenna and Yagi-Elements

Since there was no visible and substantial difference with the introduction of a reflector element, the height between the Yagi-elements and the antenna was increased. Fig. 24 illustrates the new modification.

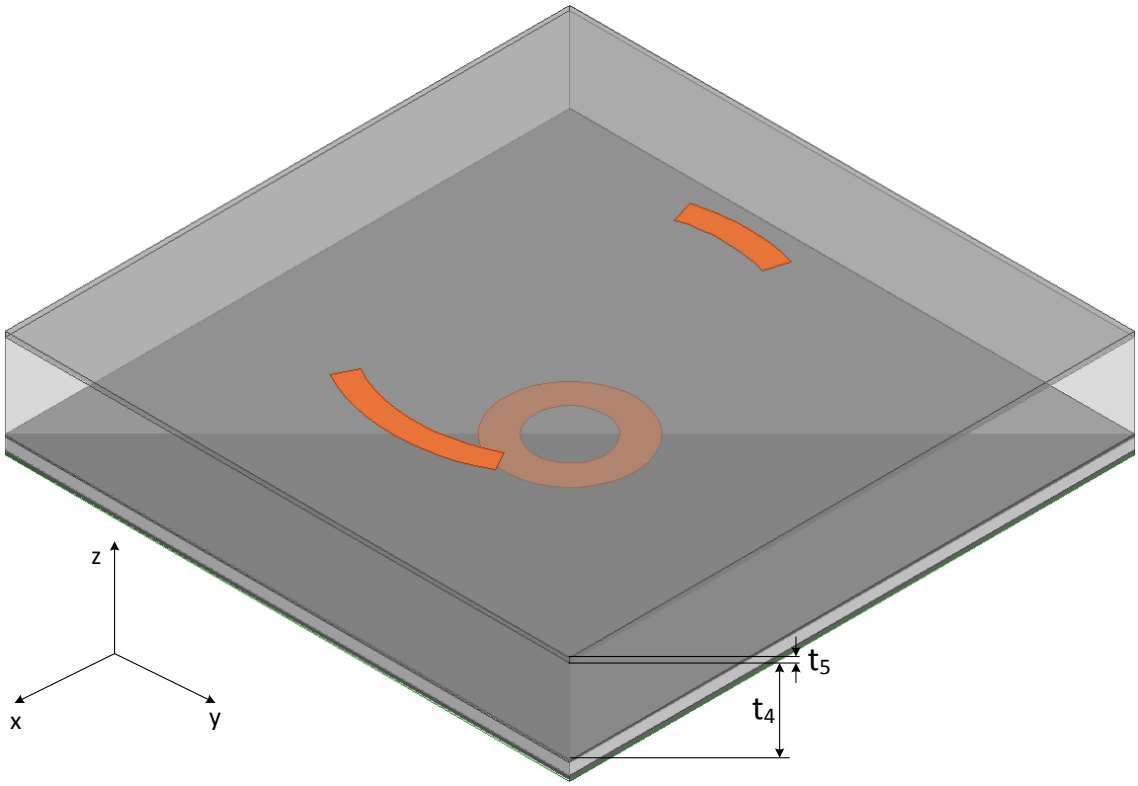

Fig. 24. HFSS 3D model, depicting a foam layer that separates the Yagi-elements and the stacked ARMSP antenna. The shorter element (towards the right) is the director and the longer element (towards the left) is the reflector.

After fine-tuning the design with the following parameters shown in Table 3, a beam-tilt of 30° towards the negative x-axis was observed while still maintaining

acceptable levels of port reflections. S parameter plots are shown in Fig. 25. Radiation pattern is presented in Fig. 26.

Table 3. Design parameters for Quasi-Yagi Stacked ARMSP antenna with a Director-Reflector configuration.

Design Parameter	Value
Substrate-1 thickness (t_1)	1.5748 mm
Foam thickness (t_2)	4 mm
Substrate-2 thickness (t_3)	0.787 mm
ARMSP-1 inner radius (a_1)	9 mm
ARMSP-1 outer radius (b_1)	20.5 mm
ARMSP-2 inner radius (a_2)	12.5 mm
ARMSP-2 outer radius (b_2)	23 mm
Probe feed location (from origin)	11.5 mm
Foam thickness (t_3)	30 mm
Substrate-3 thickness (t_5)	1.5748 mm
Reflector Spacing ($spacing_r$)	59 mm
Director Spacing ($spacing_d$)	59 mm
Reflector width (w_r)	8 mm
Director width (w_d)	8 mm
Reflector arc length	57 mm
Director arc length	34 mm

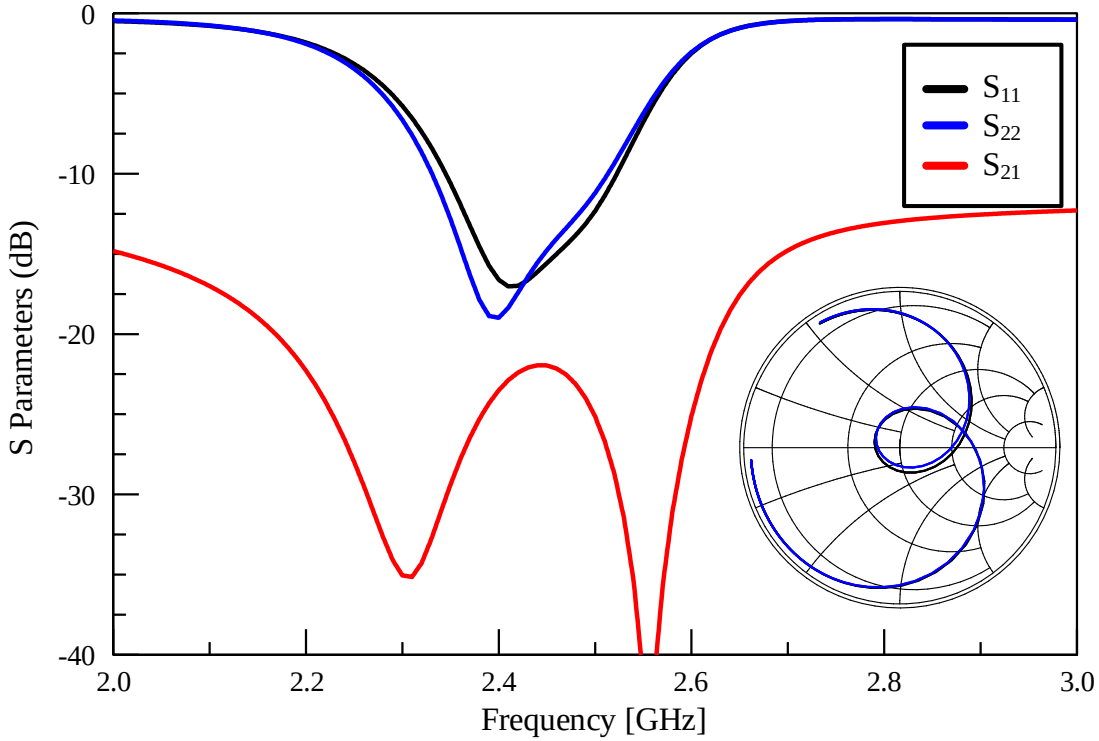

Fig. 25. Port reflection parameters showing acceptable impedance matching across the desired bandwidth and strong isolation between the two feed ports.

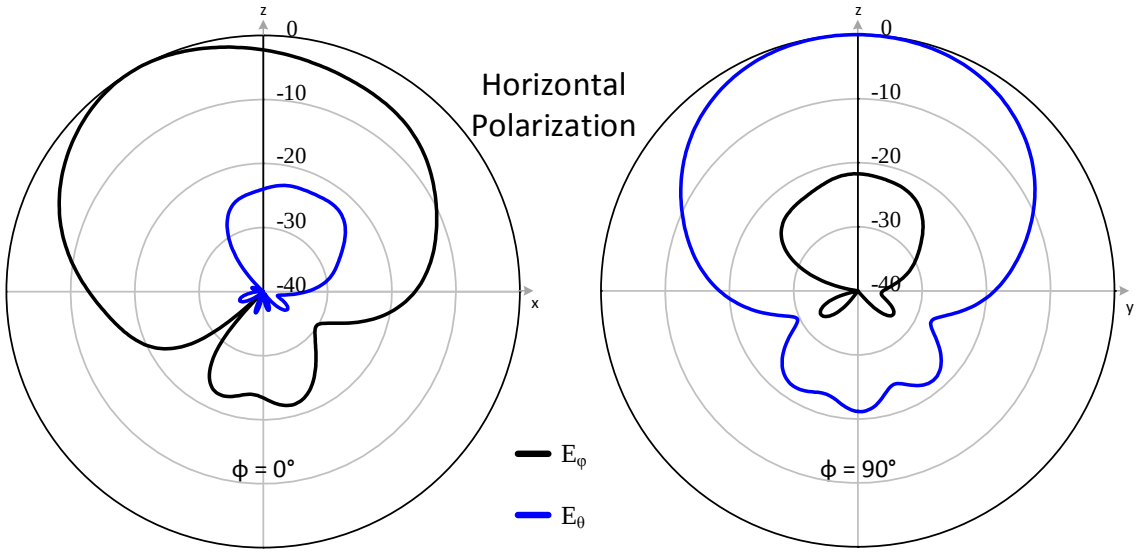

Fig. 26. Normalized radiation pattern showing fields for horizontal polarization

4.2 Pattern Reconfigurable Quasi-Yagi Coupled Stacked ARMSP Antenna

In the previous sub-section, the ability for the radiated main beam to skew from the broadside direction was established. This sub-section details the strategies and design changes adopted for being able to electronically control the pattern across both polarizations.

4.2.1 Use of RF PIN Diodes to Switch between Director and Reflector

The ability to achieve pattern reconfiguration with the help of RF PIN diodes was established in [4] and [5]. The similar concept is being investigated here.

In the previous sub-section, the Yagi-elements were fixed to be either a director or reflector, and with that configuration, only a certain type of radiation pattern was observed. If the director and reflector were interchanged, the main beam would skew towards the positive x-axis instead of the negative. Therefore, in order to control the physical length of the Yagi-elements, RF PIN diodes [12] were used. That configuration is illustrated in Fig. 27, where each diode shown is representative of two diodes places near the edges of the parasitic elements. For the sake of understanding the pattern behavior, DC bias lines were not simulated.

The diodes are oriented in such that the anodes are pointing inwards to every element. A small gap is introduced so as to position the diodes and to keep the main element open-circuit from the edges. When the diodes are forward biased, as per the data sheet [12], they offer very minimal resistance ($R_s \approx 1.5\Omega$) and shunt capacitance ($C_s = 0.18pF$). Under reverse bias conditions, the diodes were simulated to have a

series resistance of $R_s = 15k\Omega$. All diodes have a packaging inductance and this is accounted for in the simulations with the value from the datasheet ($L_s = 0.7nH$) [12].

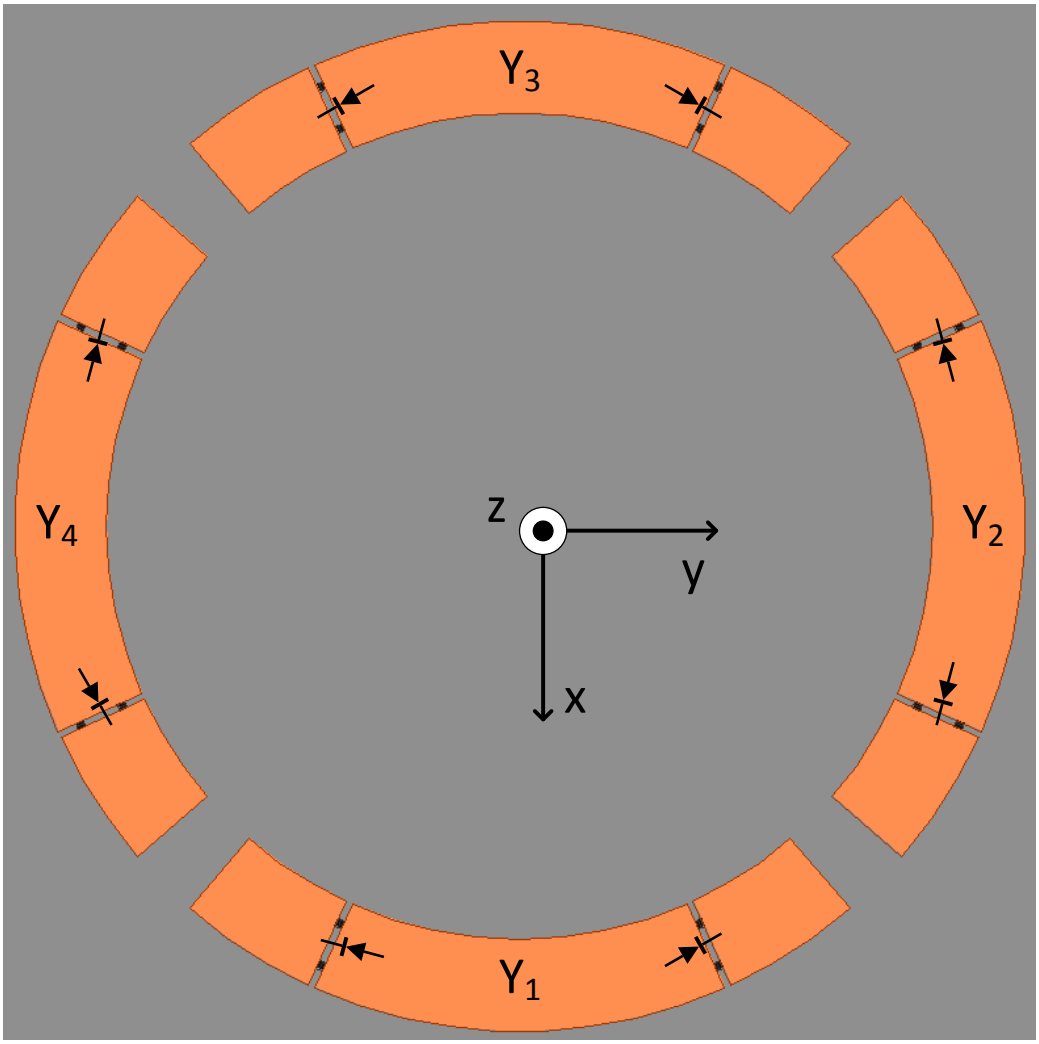

Fig. 27. RF PIN Diode configuration on the Yagi-elements to control lengths of those elements. Y_1 and Y_3 couple with feed port 2 and Y_2 and Y_4 couple with feed port 1.

With the diodes forward biased, the diodes allow the surface currents to pass through and also excite the edges of the elements, thus making it longer and therefore designed to be a reflector. However, when the diodes are reverse biased, the diodes offer very high resistance for the surface currents to flow through and only confine the currents to operate as a director.

With this environment and diodes setup, while maintaining the same reflector and director dimensions as the previous experiment, there was no observed beam-tilt for any diode state. But as the reflector and director spacing were reduced, the antenna began to couple with the Yagi-elements and the radiation patterns were affected. However, as the coupling increased, the port reflections increased too. Fig. 28 presents the reflections at the ports at a reflector and director spacing of 40 mm.

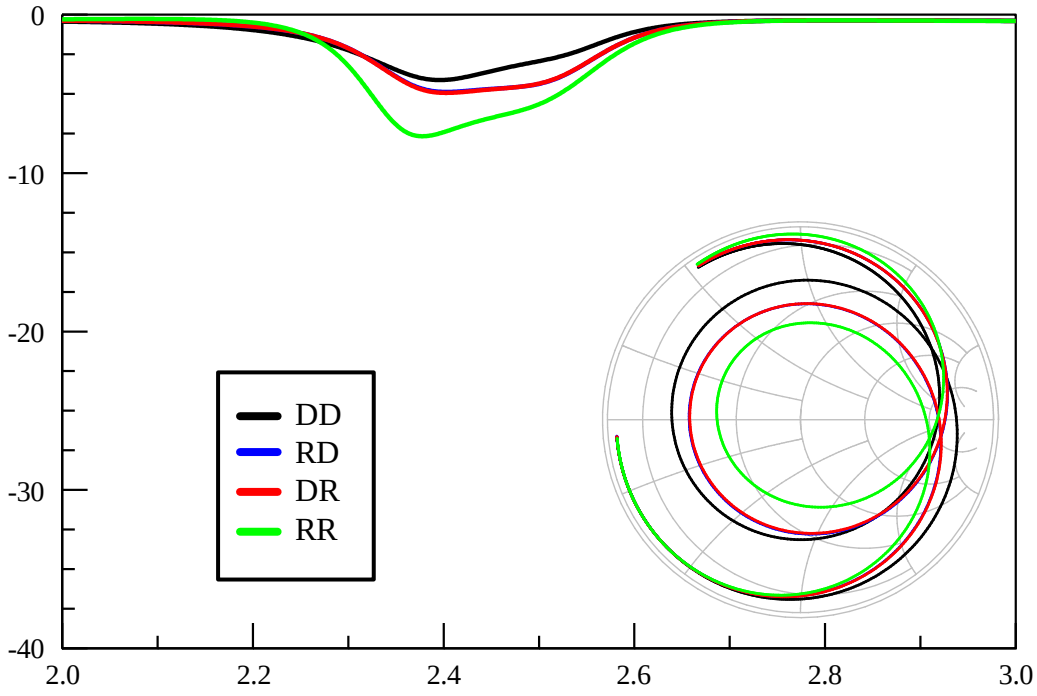

Fig. 28. Port reflection parameters for all Yagi modes affecting port 2.

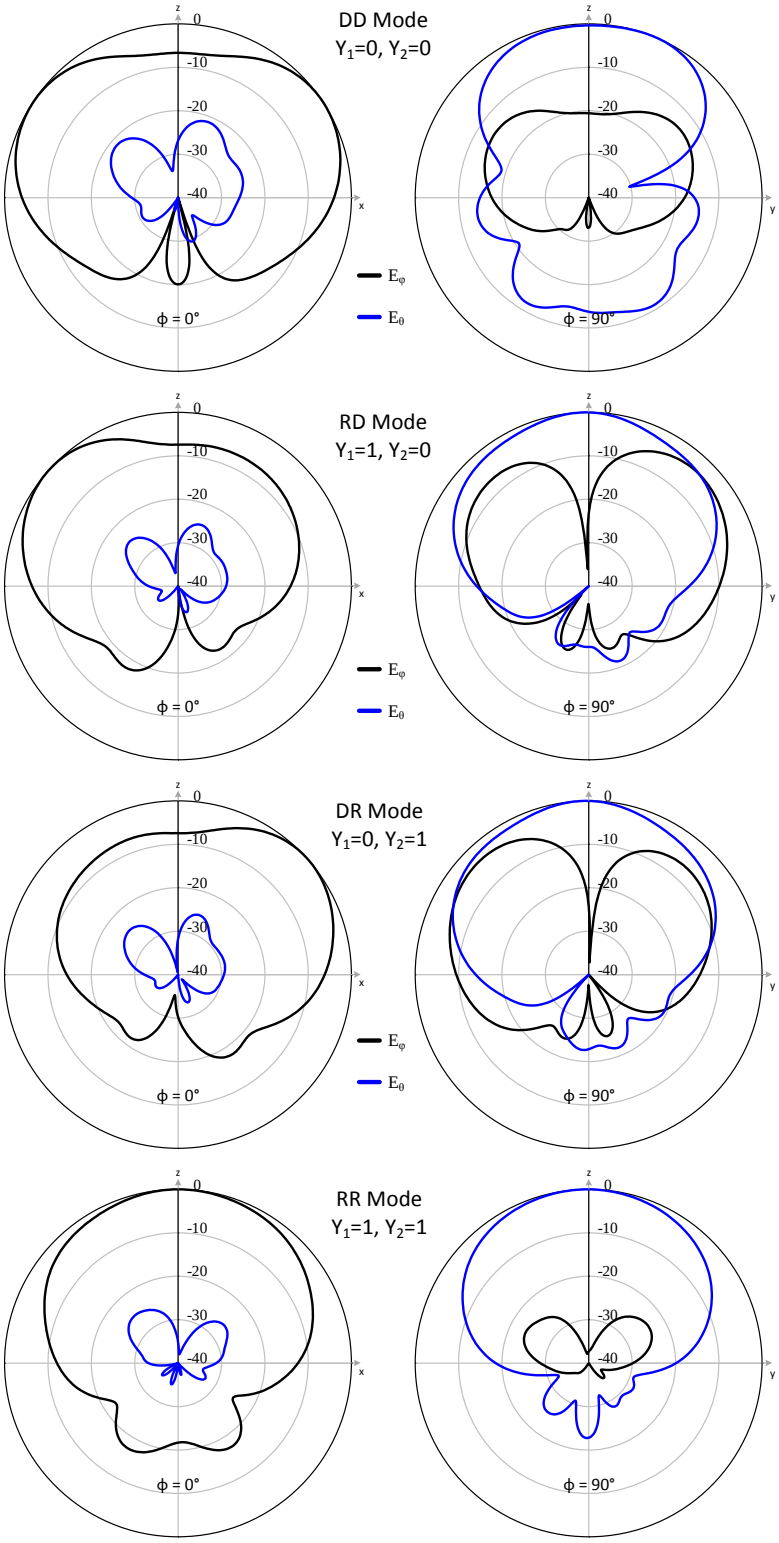

Fig. 29. Normalized radiation patterns for all Yagi modes affecting port 2.

4.2.2 Impedance Matching the Quasi-Yagi Pattern Reconfigurable Stacked ARMSP Antenna

As evident from Fig. 28, the impedance matching is lost at the expense of a high beam tilt for any of the modes involving the director. There were various methods used to impedance match this antenna, viz., quarter wave transformer (QWT), stub matching, and changing the probe feed position.

At frequencies close to 2.45 GHz, the impedance was very close to the real axis of the Smith chart. So in order to impedance this, a quarter wave transformer was used. This was achieved by probe-feeding into a transmission line designed as a QWT, and with a length of $\frac{\lambda_g}{4}$. This solution was not feasible due to the narrow-band nature of a QWT and the feeding mechanism from a probe to a microstrip line was highly inefficient.

Placing stubs on the outer periphery as well as the inner periphery helped but the results were not broadband enough to cover the required bandwidth. Changing the probe feed position, however, adversely affected the frequency of resonance of the antenna; the closer it was the inner periphery, the lower the frequency of resonance. Hence, none of these mechanisms worked well enough to solve the issue.

Just as how the impedance performance of the first layer ARMSP improved upon adding a second layer ARMSP, a similar approach was tried, but with a circular disk instead. Fig. 30 illustrates this design. The radius of this disk was set to be $21mm$.

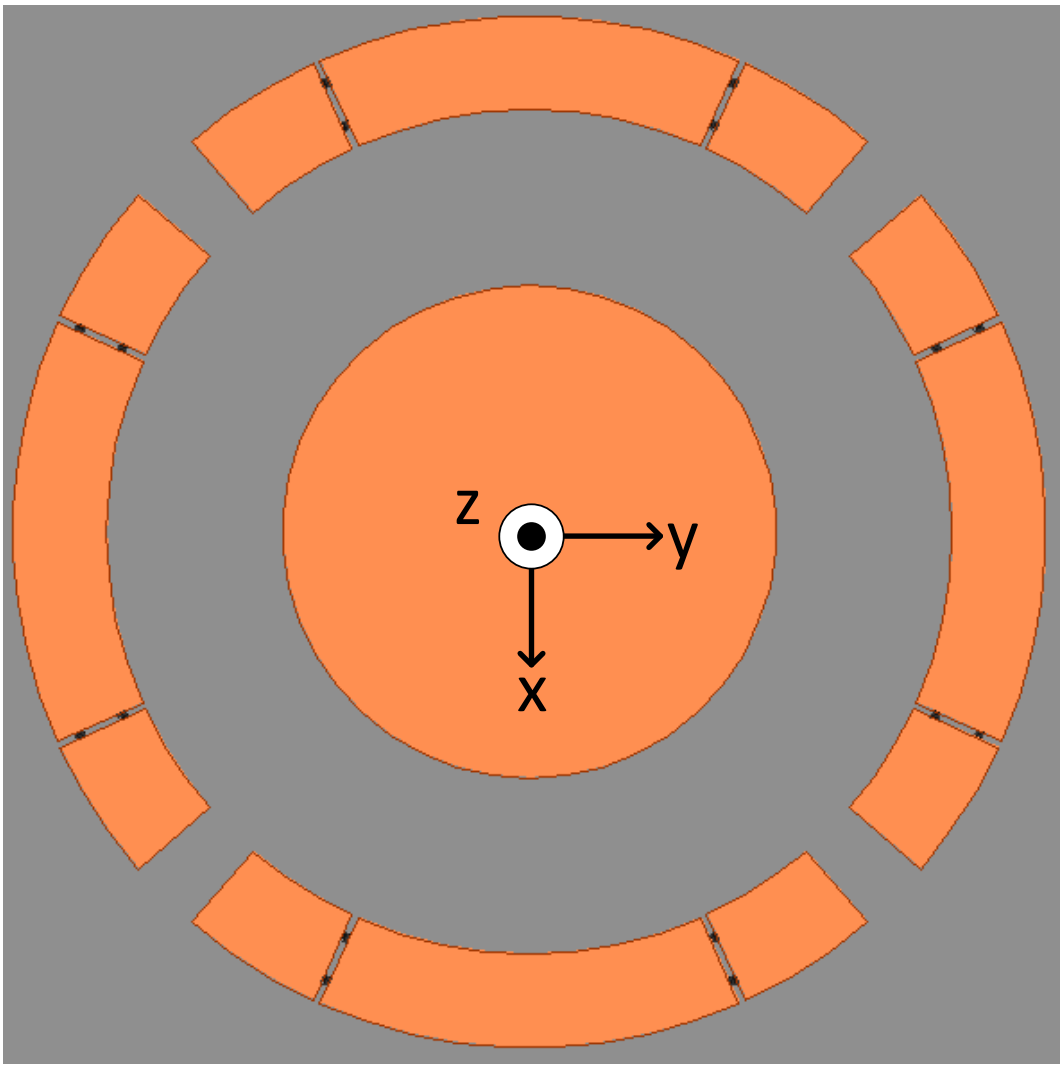

Fig. 30. Illustration of a Circular disk loaded Quasi-Yagi Pattern Reconfigurable Stacked ARMSP antenna.

Fig. 31 presents the port reflection parameters. Except for the RR mode, all the impedance bandwidths look agreeable. Fig. 32 presents the radiation pattern results.

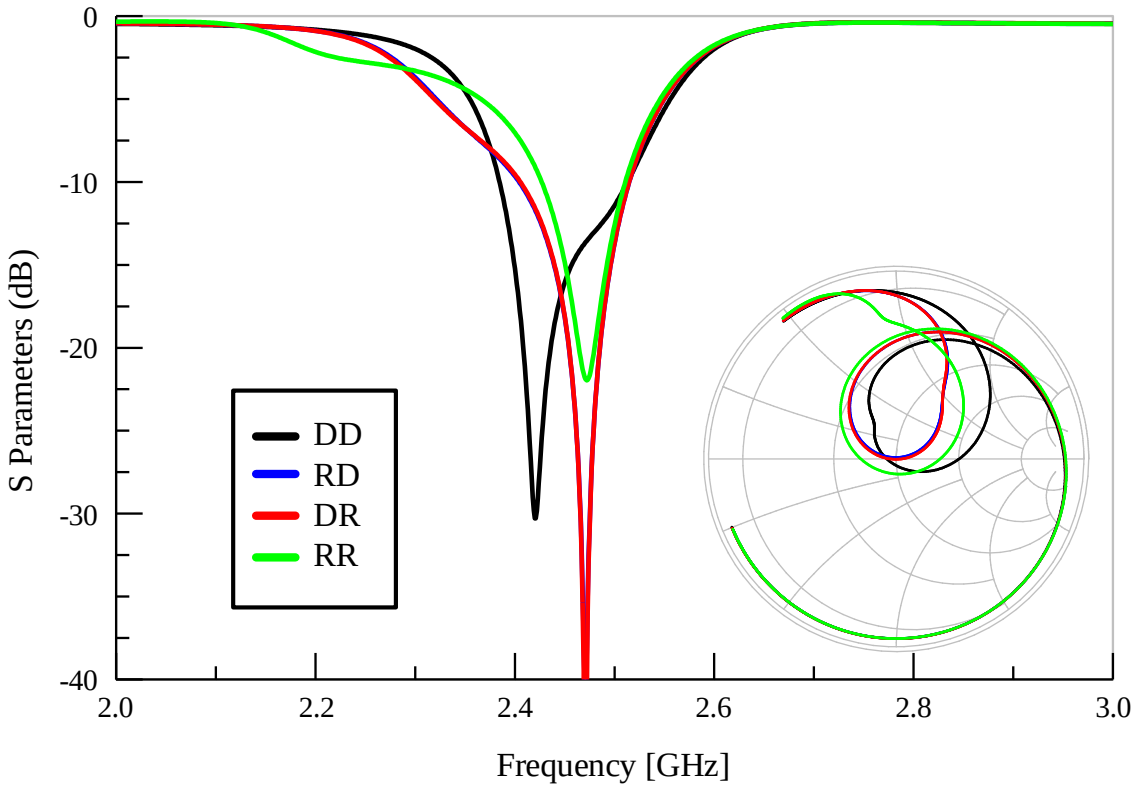

Fig. 31. Port reflection parameters for all modes on Y_1 and Y_3, when excited by port 2.

Though this design improves upon the port impedance matching, it still does not provide the right bandwidth for all the modes. The beam tilts for the RD or DR modes are not as distinct as those obtained in Fig. 29.

As mentioned, the other important take away from this investigation is that when the antenna couples with different modes, due to the lengths of the Yagi-elements, the resonant frequency shifts, thus altering the bandwidth of operation. This design, therefore, required a broader-band response such that the frequency shift due to the Yagi elements would still lie within the frequency response of the antenna, while maintaining the desired impedance bandwidth.

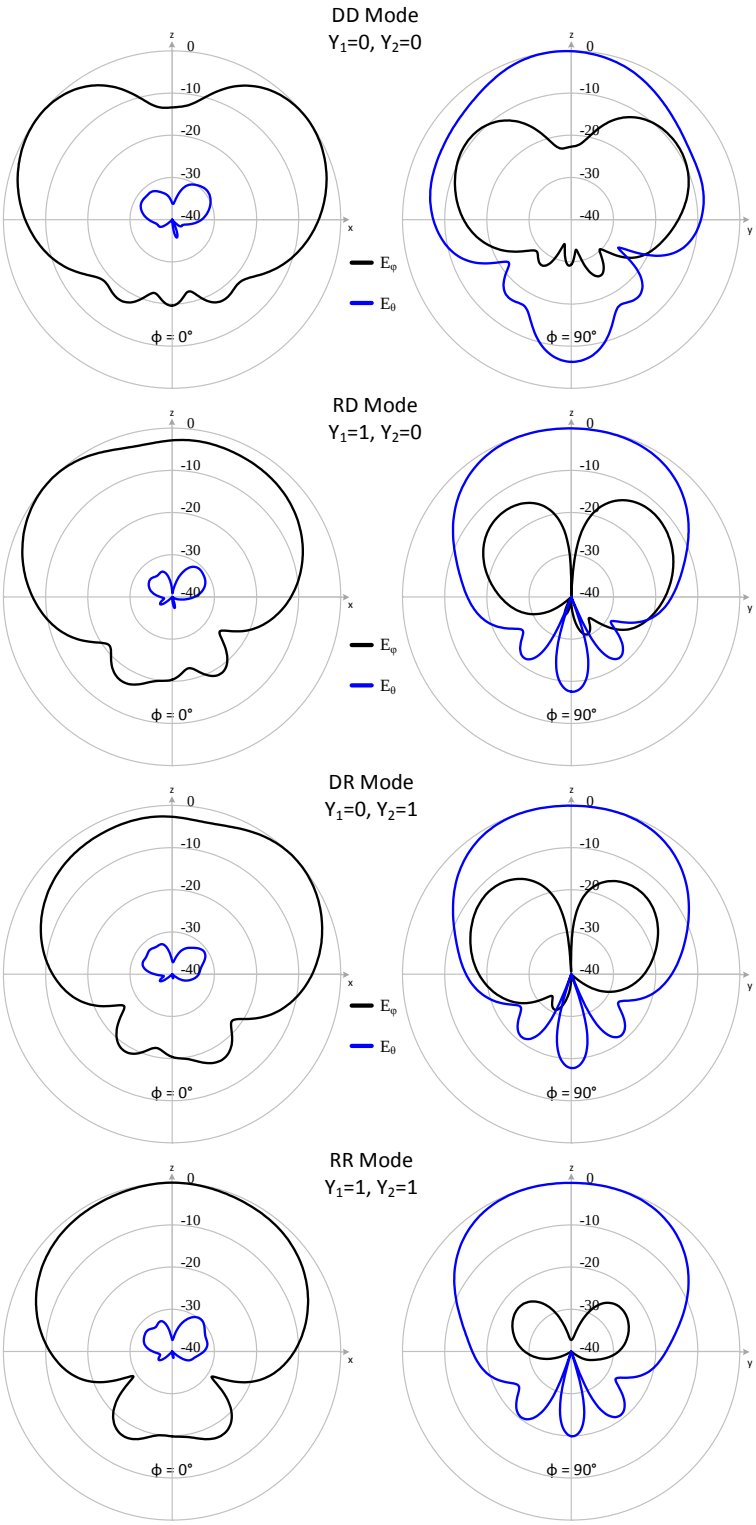

Fig. 32. Normalized radiation patterns for design with the circular disk loading for all Yagi modes.

CHAPTER V

IMPROVEMENTS ON PATTERN RECONFIGURABLE BROADBAND ANNULAR RING PATCH ANTENNA

5.1 Improving Radiating Element Broadband Response on Duroid 5870 Substrate

In the previous section, it was understood that a third layer of patch (circular disk) needs to be present (on the same plane as the Yagi-elements) in order to maintain a good reflection coefficient behavior. This, however, was achieved at the cost of losing out on the extent of the beam tilt angle, possibly due to the broadside radiation characteristics of the circular disk. Efforts were then made to optimize the shape of the third layer of the patch. This was done on substrate duroid 5870, as mentioned earlier, due to the unavailability of duroid 5880. The design had to be, initially, modified to resonate at 2.45 GHz without the Yagi-elements. This was achieved and reported in section 3.4. It was for the reason stated above why the bandwidth of the stacked ARMSP antenna was allowed to be kept much higher than required.

Extensive simulations had to be performed to obtain the optimum dimensions of the Yagi-elements and the design parameters are tabulated in Table 4.

Table 4. Design parameters for pattern reconfigurable Quasi-Yagi Stacked ARMSP Antenna with broadband characteristics and improved reflection coefficients.

Design Parameter	Value
Substrate-1 thickness (t_1)	1.5748 mm
Foam thickness (t_2)	4.5 mm
Substrate-2 thickness (t_3)	1.5748 mm
ARMSP-1 inner radius (a_1)	7.5 mm
ARMSP-1 outer radius (b_1)	20.5 mm
ARMSP-2 inner radius (a_2)	10 mm
ARMSP-2 outer radius (b_2)	23 mm
Probe feed location (from origin)	12 mm
Foam thickness (t_3)	24 mm
Substrate-3 thickness (t_5)	0.508 mm
Reflector Spacing ($spacing_r$)	44 mm
Director Spacing ($spacing_d$)	44 mm
Reflector width (w_r)	8 mm
Director width (w_d)	8 mm
Reflector arc length	54 mm
Director arc length	36 mm

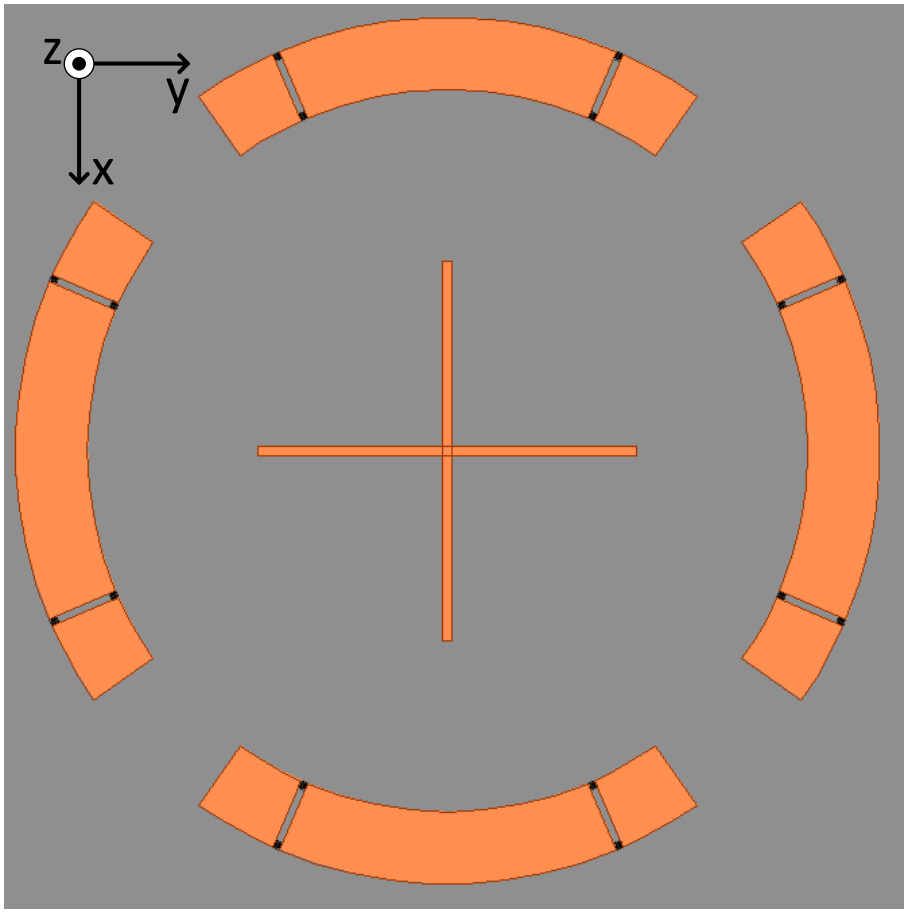

Fig. 33. Illustration of design of the third patch element (as a replacement to the circular disk).

Fig. 34 presents the port reflection parameters for all modes and Fig. 35 presents the radiation patterns for this design.

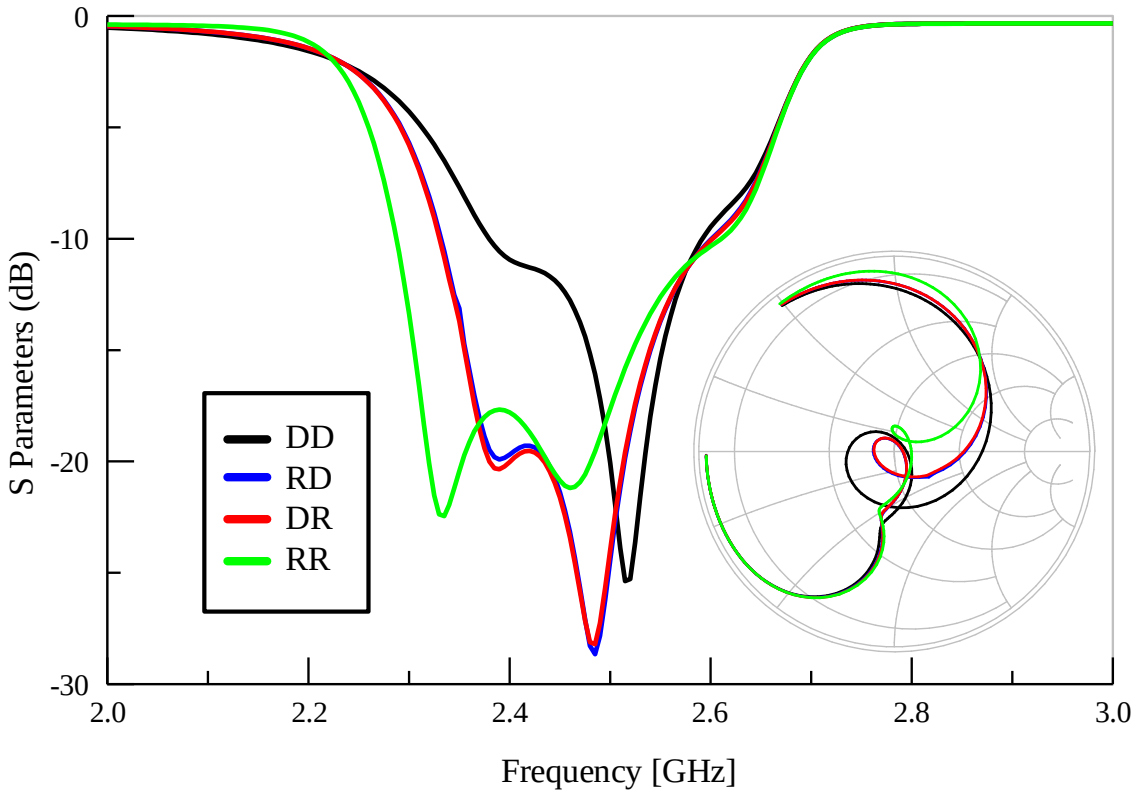

Fig. 34. Port reflection parameters for the third patch element as a cross structure. Shown are all modes on Y1 and Y3 when excited by port 2.

It can be observed in Fig. 35 that in the DD mode, the main beam tilts to approximately ±55°. In the DR and RD modes, the tilt is nearly +45° and –45° respectively, with about a 5dB decrease in gain on the opposite side. The RR mode makes the antenna behave as a traditional microstrip patch antenna with the main beam at broadside.

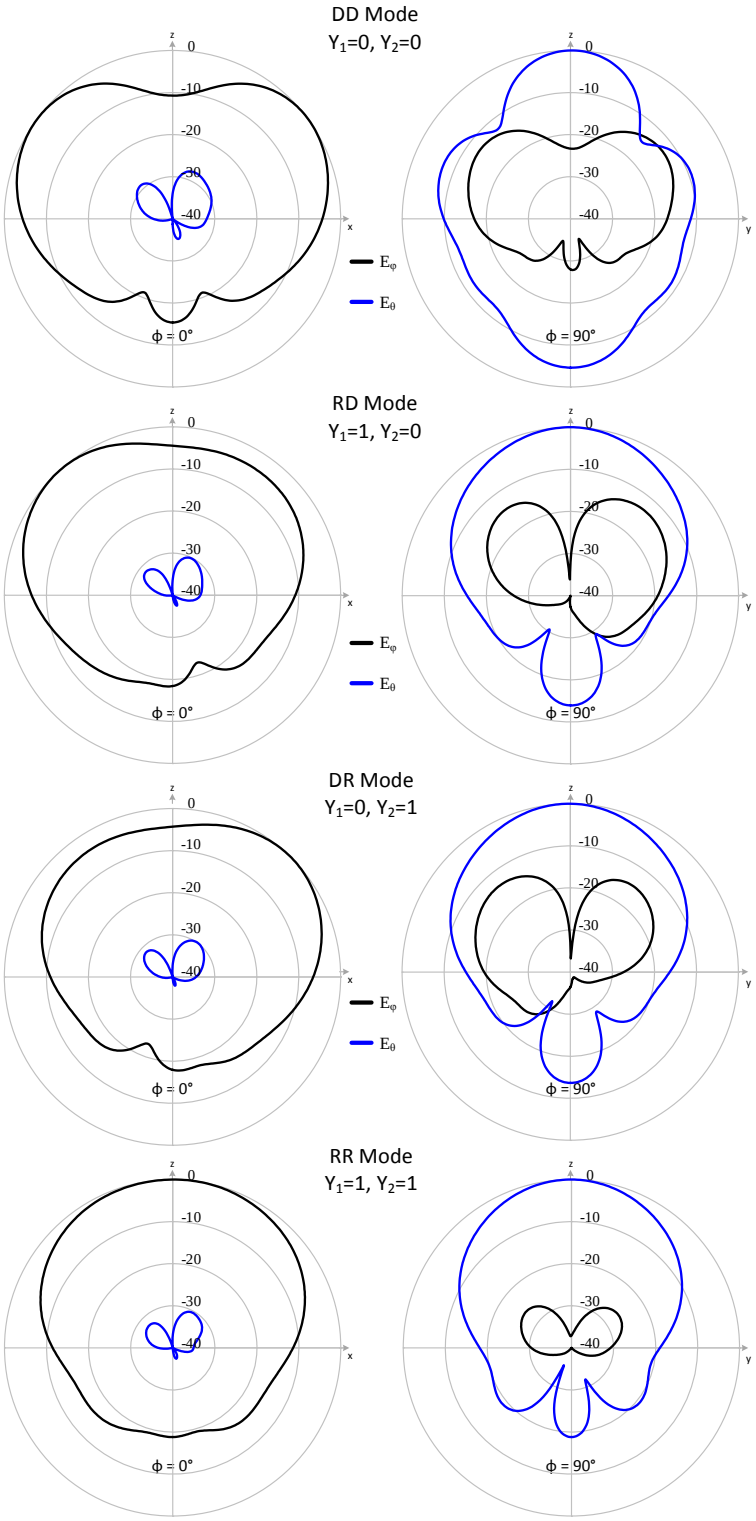

Fig. 35. Normalized radiation patterns for design with crossed microstrip line loading for all Yagi modes.

5.2 Design of DC Lines for RF PIN Diode Biasing

So far, the design has considered just microstrip RF radiating elements with an RLC model of diodes, simulating their ON and OFF states. Since these diodes need to be biased in order to behave as switches, DC feed lines have to be designed.

Just having wires or copper strips feeding into these Yagi elements wouldn't be a wise decision, because as explained in section 5.1, having a resonant length element of thickness $< 0.009\lambda_g$ had a significant effect on the port reflection parameters.

5.2.1 First Iteration with RF Open-Circuit Cross-Coupled Lines

The main driving force behind this was to have as few DC feed lines as possible. Fig. 36 illustrates these feed lines, showing just one half of the antenna.

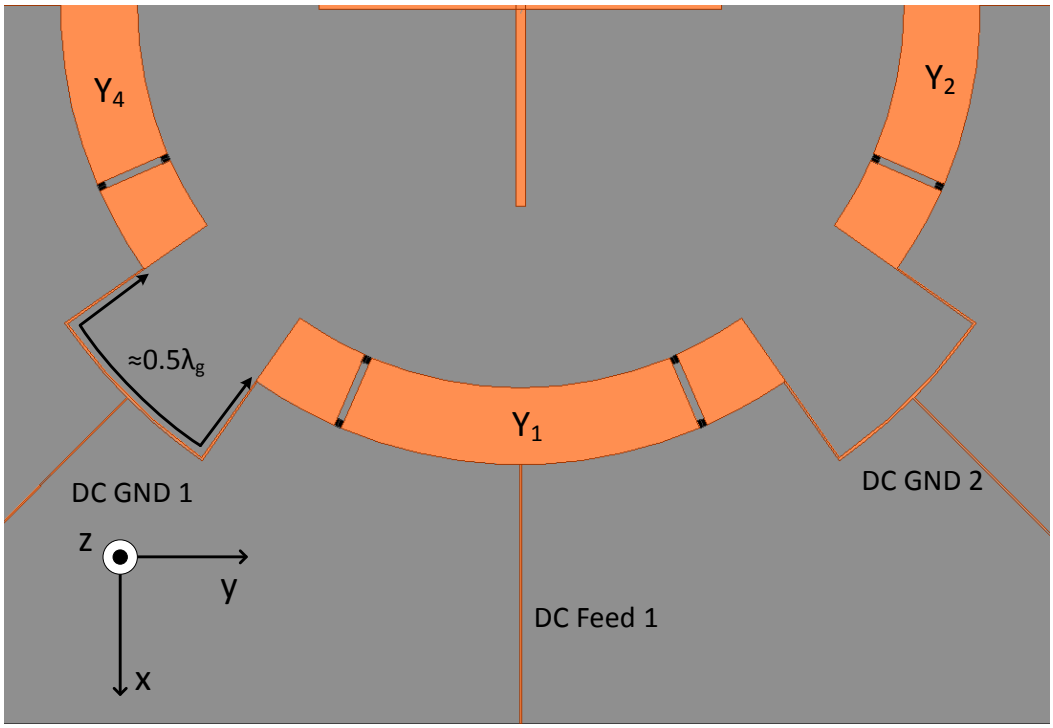

Fig. 36. Design of the DC feed lines.

Since the ends of the Yagi elements represent an RF open-circuit, travelling $0.5\lambda_g$ on a transmission line will bring the impedance back to an RF open-circuit. Upon simulating this, the port reflection parameters were affected, bringing the reflection coefficient down to about -7dB. The radiation pattern was not as distinct as without the DC lines. It was then observed that though Y_1 and Y_4 are open-circuit, there is still some amount of surface current leaking into the other polarization element. This was avoided with the help of an inductor behaving as an RF choke, and the cross-connected design was not opted for.

5.2.2 Second Iteration with Meandering DC Feed Lines

When port 1 is activated, Y_2 and Y_4 are coupled. Along with this, since the "DC Feed 1" line is oriented in the same direction, it is also coupled and distorts the intended operation. To solve this issue, a meandering DC feed line was introduced. Fig. 37 illustrates this design.

Fig. 38 presents the port reflection parameters for all Yagi modes. Fig. 39 presents the radiation patterns for those modes. From Fig. 39, it is clear that having meandering feed lines has improved the radiation performance as well as reduced the coupling with the radiating elements.

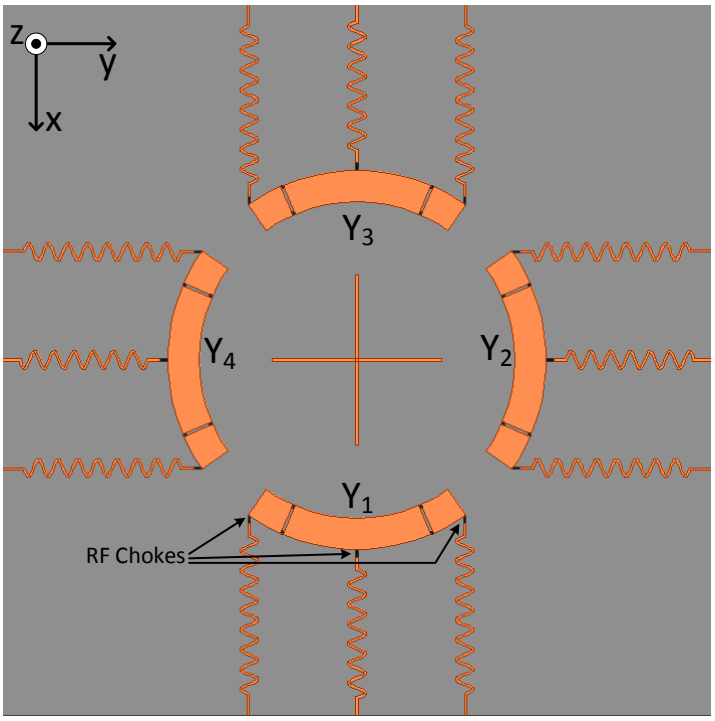

Fig. 37. Design illustrating meandering feed lines and RF chokes.

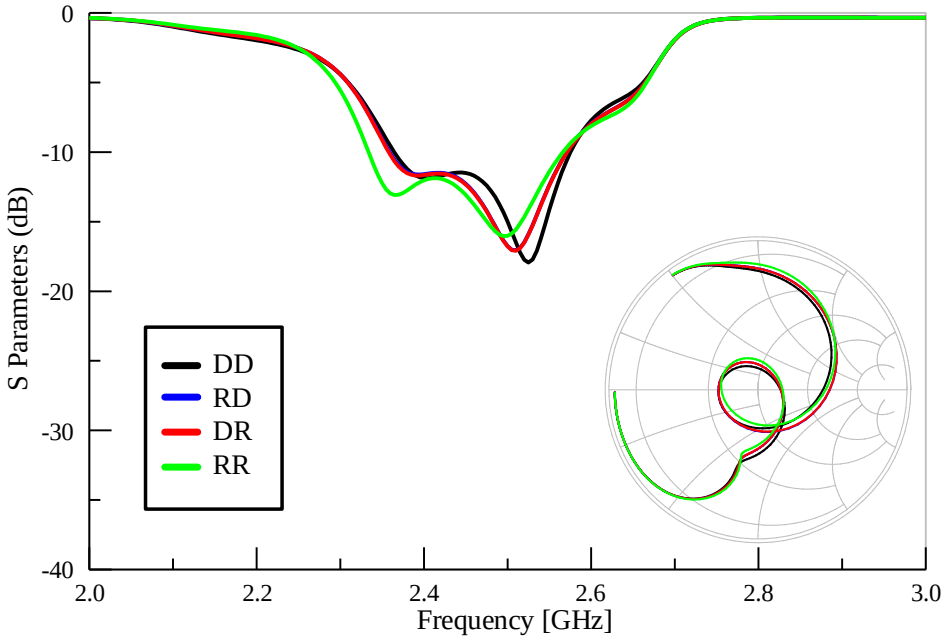

Fig. 38. Port reflection parameters for the meandering DC feed lines design. All modes are sufficiently well matched.

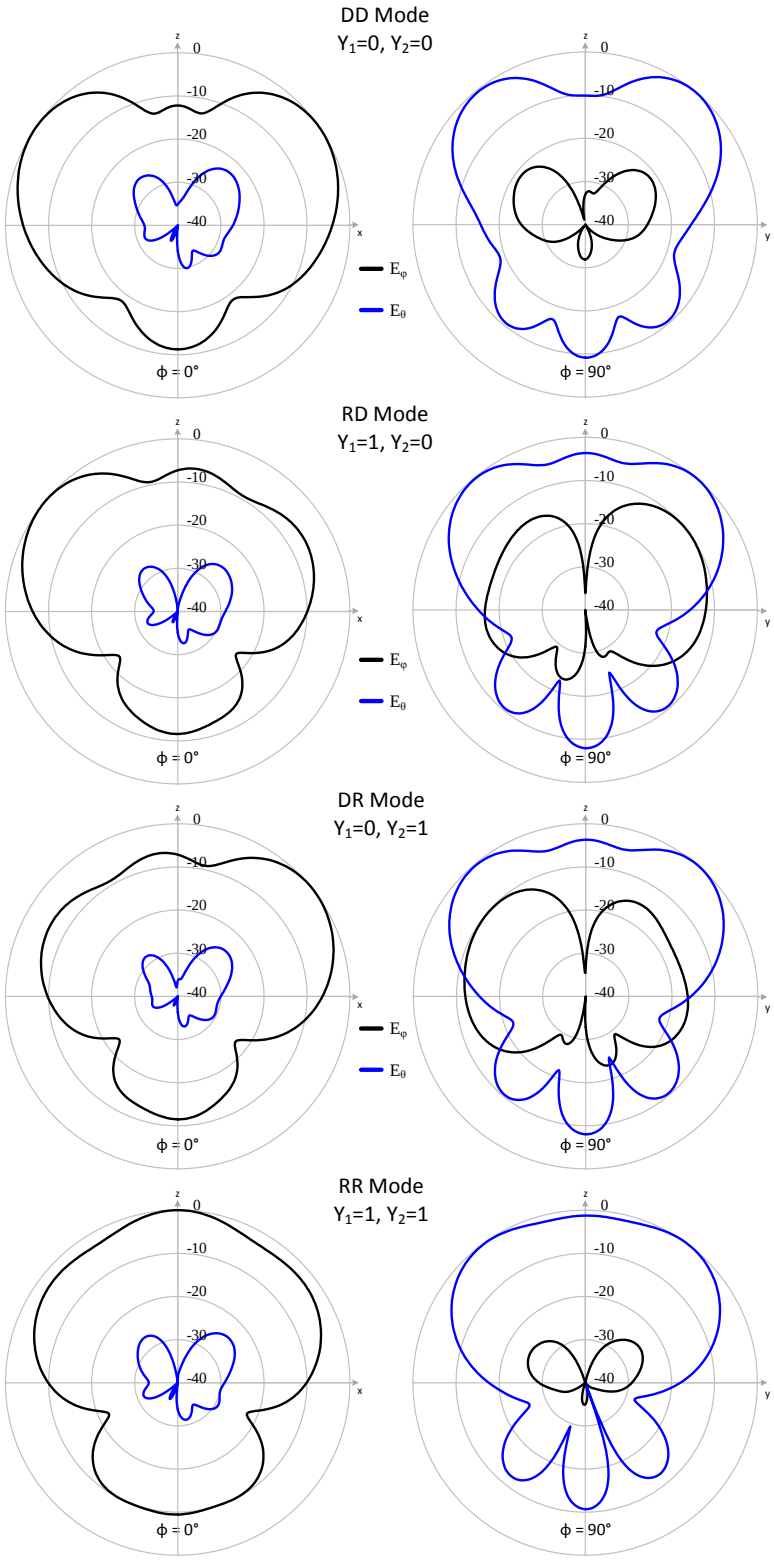

Fig. 39. Normalized radiation patterns of antenna with meandering DC feed lines.

5.3 Antenna Fabrication and Measurements

With the design presented in the previous section, the antenna was fabricated and its performance was measured.

5.3.1 Fabricated Stacked Patch Antenna with Meandering DC Feed Lines

Fig. 40 shows the fabricated top layer of the antenna. In this antenna, the horizontal Yagi-elements are unaltered and closely resemble the simulated design. The vertical Yagi-elements are, however, modified with copper tape in order to finely tune the lengths. The radiation pattern results of the unaltered fabricated antenna are presented in Fig. 41, with a comparison to the simulated results.

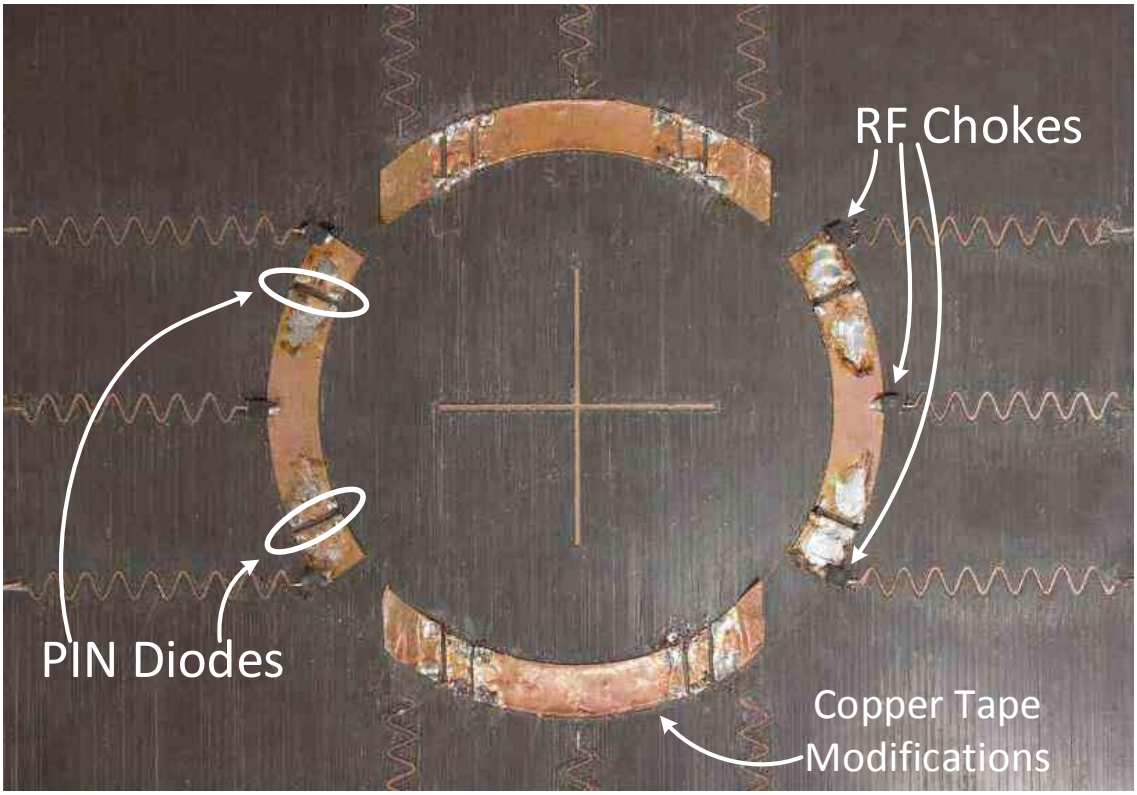

Fig. 40. Fabricated version of the meandering DC feed line top layer

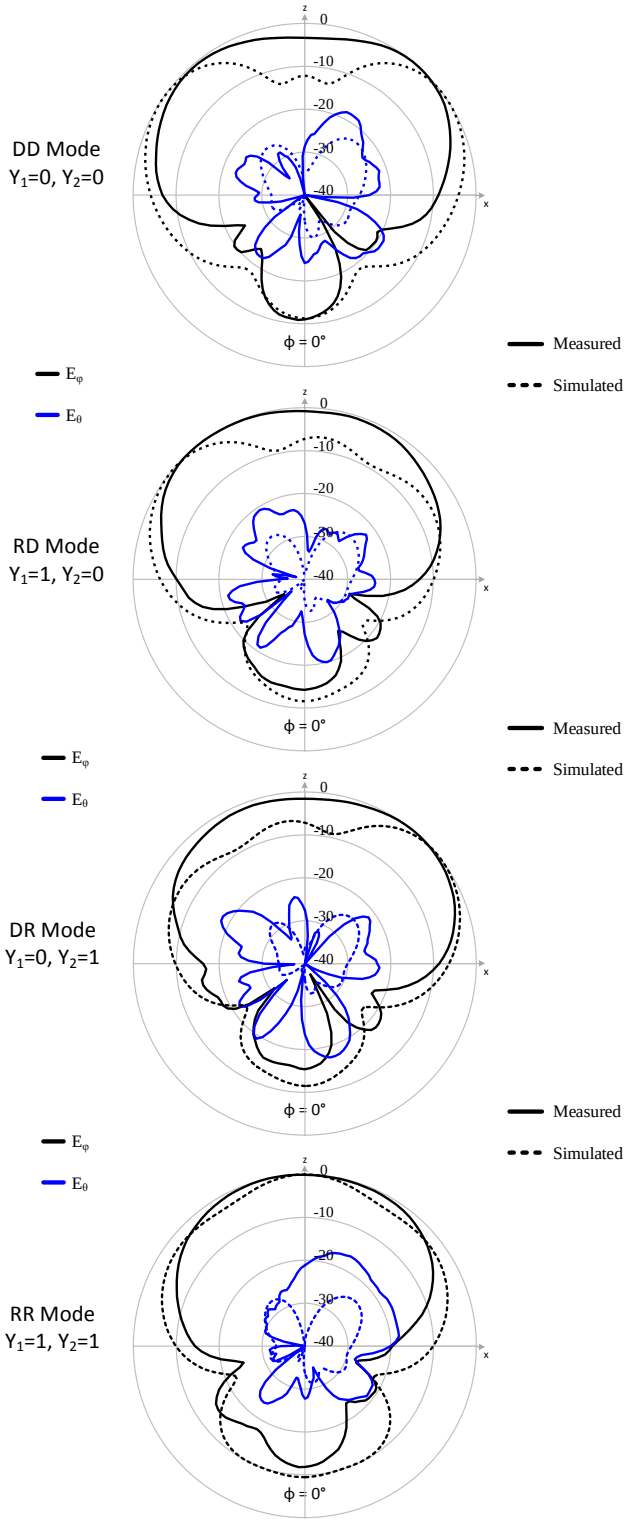

Fig. 41. Normalized radiation patterns of meandering DC feed lines Measured vs. Simulated.

From Fig. 41, the beam tilts observed were not as large an angle as the simulations. The amount of increased gain for DR or RD modes were also not as prominent as expected.

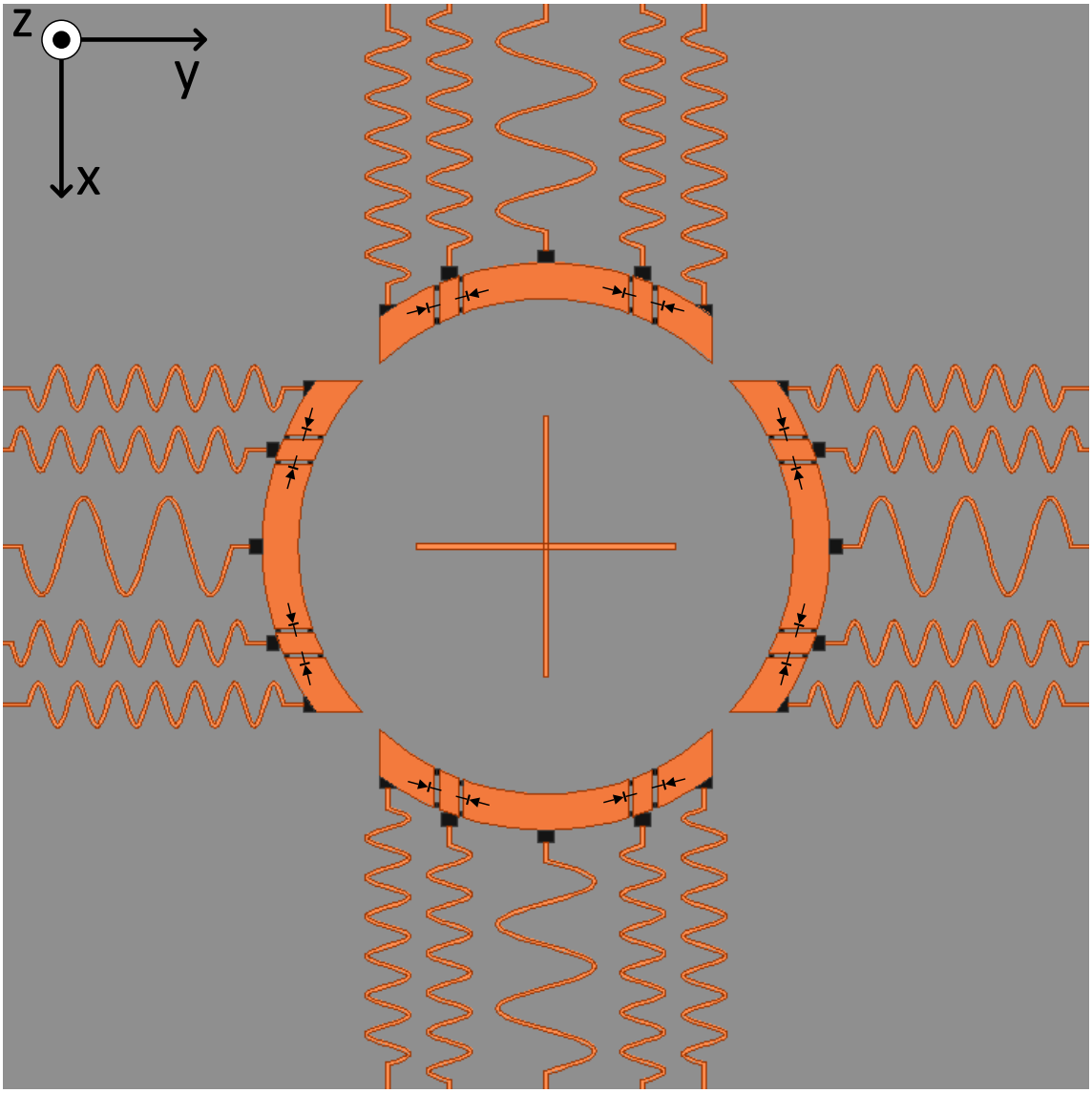

Fig. 42. CAD model of tri-state Yagi-elements with diode configurations illustrated.

It was at this point where the next stages involved copper tape. The effects of the lengths of director and reflector were investigated using copper tape and it was observed that for the design that was fabricated, the measured results matched the simulations at a frequency of 2.3 GHz. It was then understood that the director that was fabricated was electrically large for 2.45 GHz and hence yielded good results at lower frequencies (as frequency and wavelength are inversely proportional).

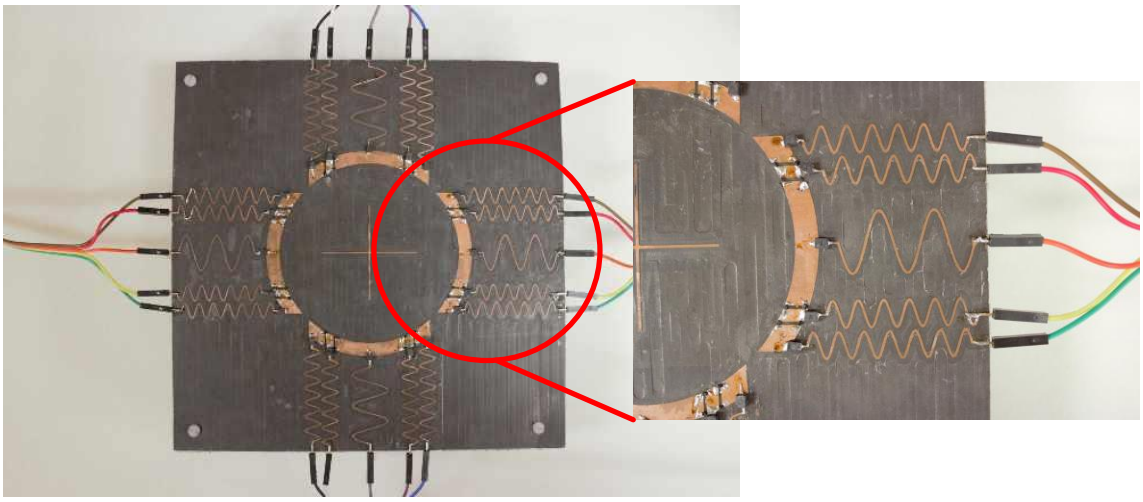

Fig. 43. Fabricated version of the meandering DC feed lines with tri-state Yagi-elements.

It was also observed that for DR or RD modes, the director needed to be shorter than for DD mode. This could be attributed to the presence of the reflector, which is a larger element, thus affecting the coupling with the director.

Taking all these factors into consideration, a newer antenna was simulated and fabricated which had the capability of switching the size of the director depending on the scenario. Fig. 42 illustrates the CAD model of this antenna and Fig. 43 shows the fabricated version of this layer. In this design, the DC feed lines were meandered with

greater magnitude and lesser frequency in order to further prevent coupling between these elements and the antenna.

Fig. 44 presents the port reflection coefficients, comparing simulated vs. measured results. Fig. 45 presents the radiation pattern results comparing simulated vs. measured results.

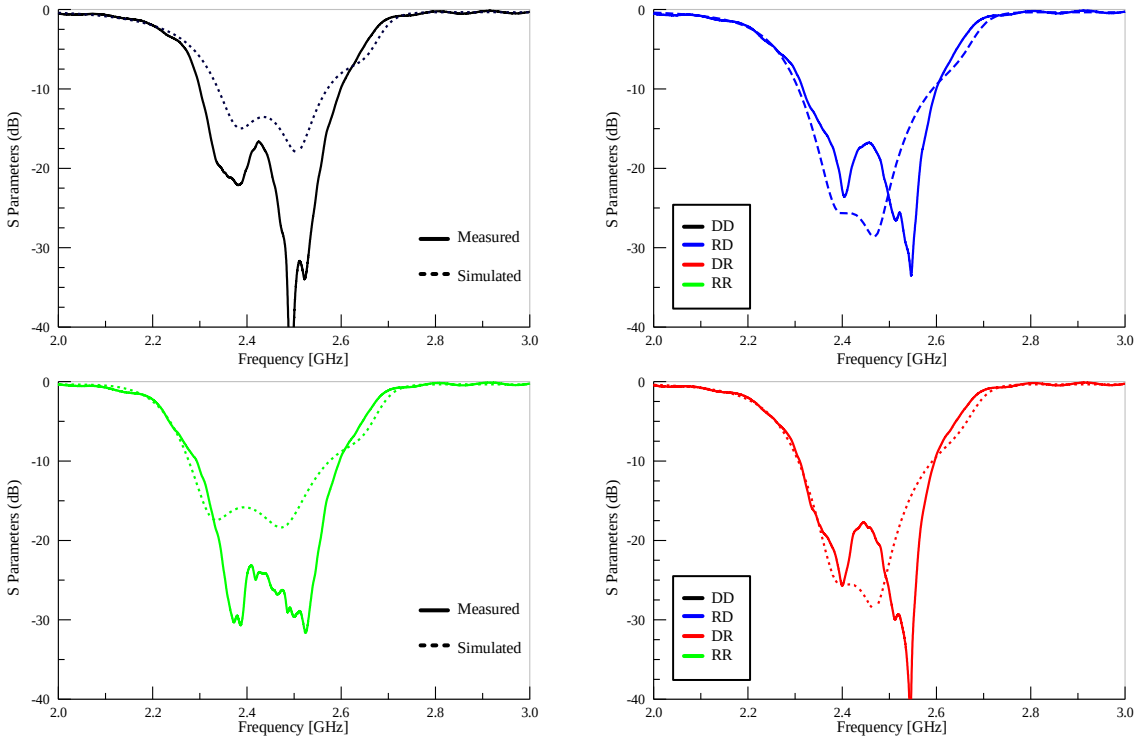

Fig. 44. Port reflection parameters comparing simulated data vs. measured.

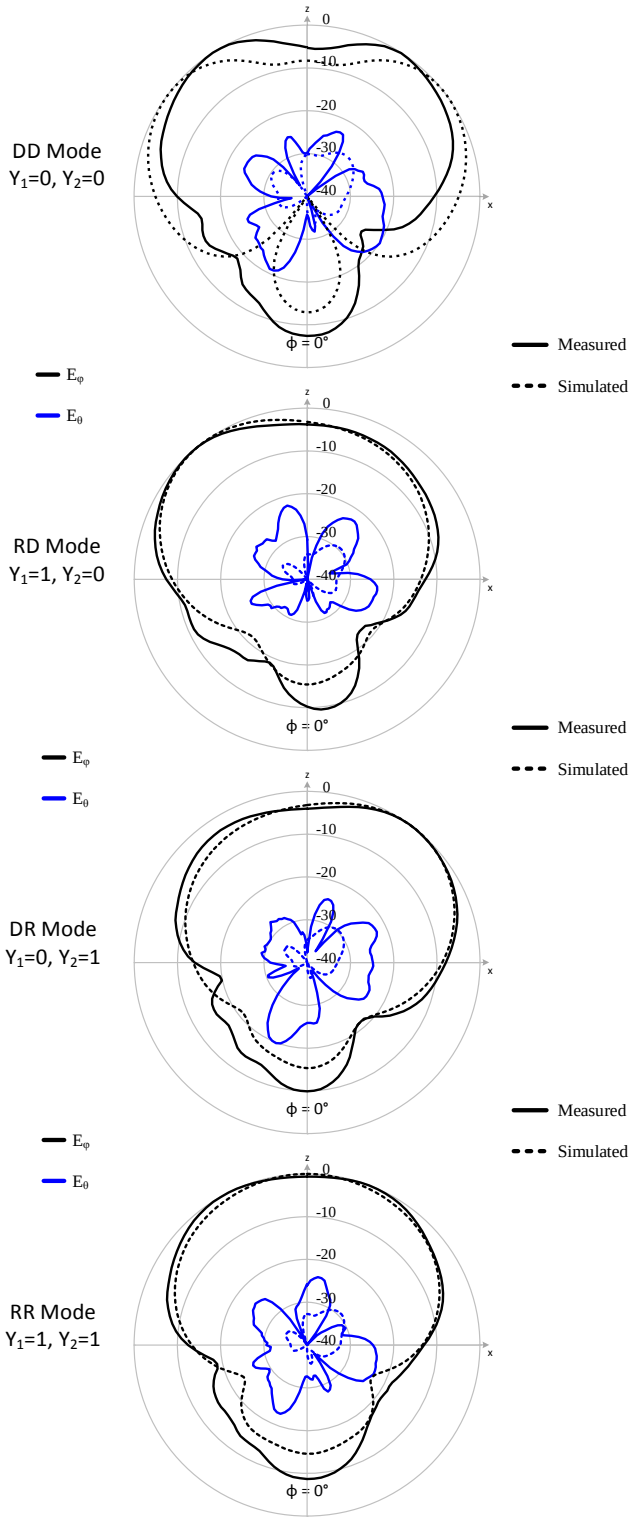

Fig. 45. Normalized radiation patterns of the tri-state Yagi-elements, simulated vs. measured.

CHAPTER VI

SOFTWARE CONTROL MECHANISM

The antenna used in [1] is a polarization reconfigurable microstrip patch antenna [2] and [3]. Polarization reconfiguration was achieved with the control of bias voltages across the diodes on both the arms of the antenna. These bias voltages could be controlled electronically, with the help of a microcontroller, along with certain electronic components such as inverters, amplifiers, etc. This chapter briefly outlines this electronic controlling mechanism along with a software program that in turn controls the microcontroller.

6.1 System Block Diagram and Working Principle

Fig. 46 depicts a brief outline of the system that is used with the reconfigurable ARMSP patch antenna, studied in this thesis. Only one control signal is depicted emanating from the microcontroller; this could, however, be multiple and independent control signals, each signal biasing diodes on the different Yagi elements as detailed in chapter 5.

The software program used in the Laptop/PC is Qt Creator, which is a cross-platform integrated development environment (IDE) that helps in creating graphical user interface (GUI) using C++ programming language. An Arduino based microcontroller, Teensy 3.1, is used to convert the control signals sent by the laptop/PC over a serial

channel, into control voltages with 0 V indicative of an OFF state and 3.3 V indicative of an ON state.

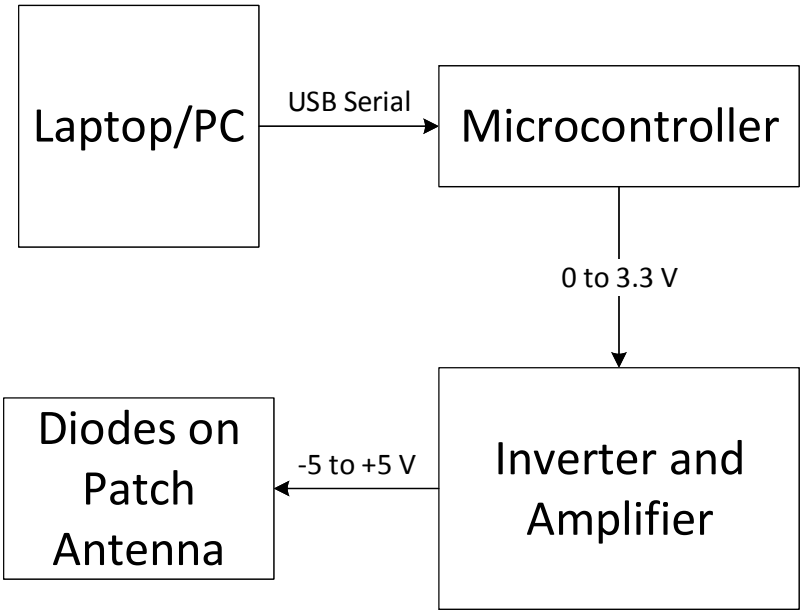

Fig. 46. Block diagram of software control mechanism for reconfigurable antenna.

An RF PIN diode, however, behaves reasonably well as an open switch (OFF state) when it is reverse biased; and for a reverse bias voltage to be achieved across the terminals, voltage difference between the anode and cathode terminals must be negative. To convert the control signals of 0 to 3.3 V into reverse and forward bias voltages, an inverter and an operational amplifier (op-amp) are used. Aside from converting the voltages to -5 V (OFF state) and +5 V (ON state), these devices also isolate the load (diodes) from the microcontroller, because these devices are directly connected to the supply voltage that drives the output. Depending on the number of independent diode

control channels required, the number of op-amps is chosen; in the case of the reconfigurable ARMSP antenna presented in chapter 5, four independent channels are necessary.

6.2 Proof-of-Concept Design and Integration with Reconfigurable SDR

To validate the design presented in section 6.1 and to implement a reconfigurable system for the antenna in [2] and [3], a software program was developed in Qt Creator that switched between the two polarization states (vertical and horizontal linear polarizations) permitted by the antenna. Since the antenna is designed such that the bias voltages are supplied along with the RF signal through the coaxial cable, an RF bias-tee is used as a diplexer (to multiplex RF and DC signals into an output port that connects to the antenna).

As a proof-of-concept, the biasing network (described in section 6.1) is setup in a Wi-Fi network with one router and one client connected to that router. As mentioned earlier, the number of control channels are governed by the required reconfiguration states; in this case, each antenna requires two channels. The antennas of both, the router and the client, are replaced with the reconfigurable antenna designed in [2] and [3], each with its own biasing network and separate bias-tees. It was observed that when the polarizations of both the antennas were oppositely aligned (cross-polarized), there was close to a 10dB drop in the recorded signal strength of the client. This behavior was then utilized to implement an auto-switching technique to orient the client to the router.

Fig. 47 shows a screenshot of the software program developed to control the antenna from the laptop/PC. The plot in the screenshot depicts the client auto-orienting itself with the router when the router changes its polarization states. The software program on the router-side was modified to switch its polarization states about every five seconds; and the software program on the client-side was modified to have an auto-switching function when a drop in received signal strength is detected.

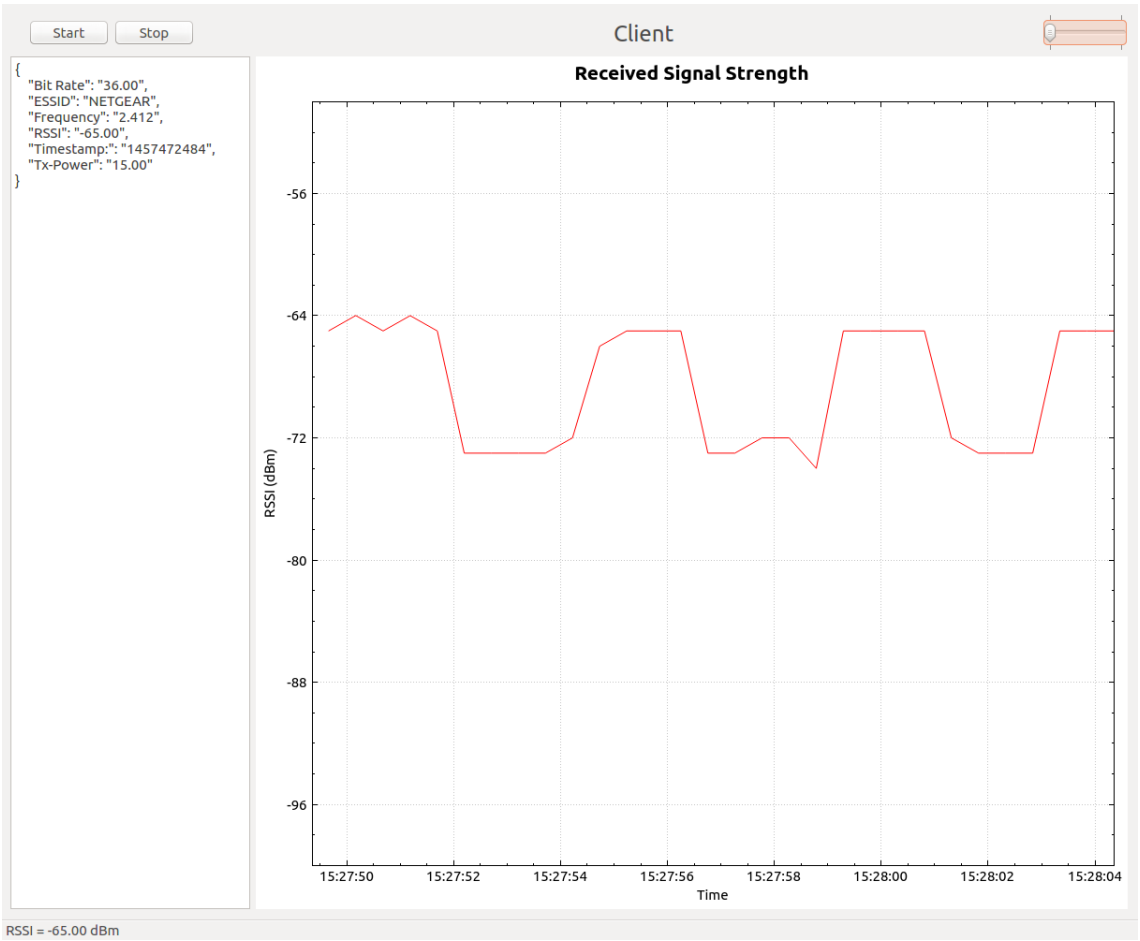

Fig. 47. Screenshot of software program depicting an auto-switching of polarization states to that of the router.

6.3 Bias Network Integration with the Reconfigurable ARMSP Antenna

With the intention that the antenna discussed in this thesis (reconfigurable ARMSP antenna) is intended to replace the antenna in [2] and [3], a modified version of the software program was developed with increased number of control channels; therefore modifications to the circuit to include increased number of amplifiers. Fig. 48 shows a screenshot of the modified software program.

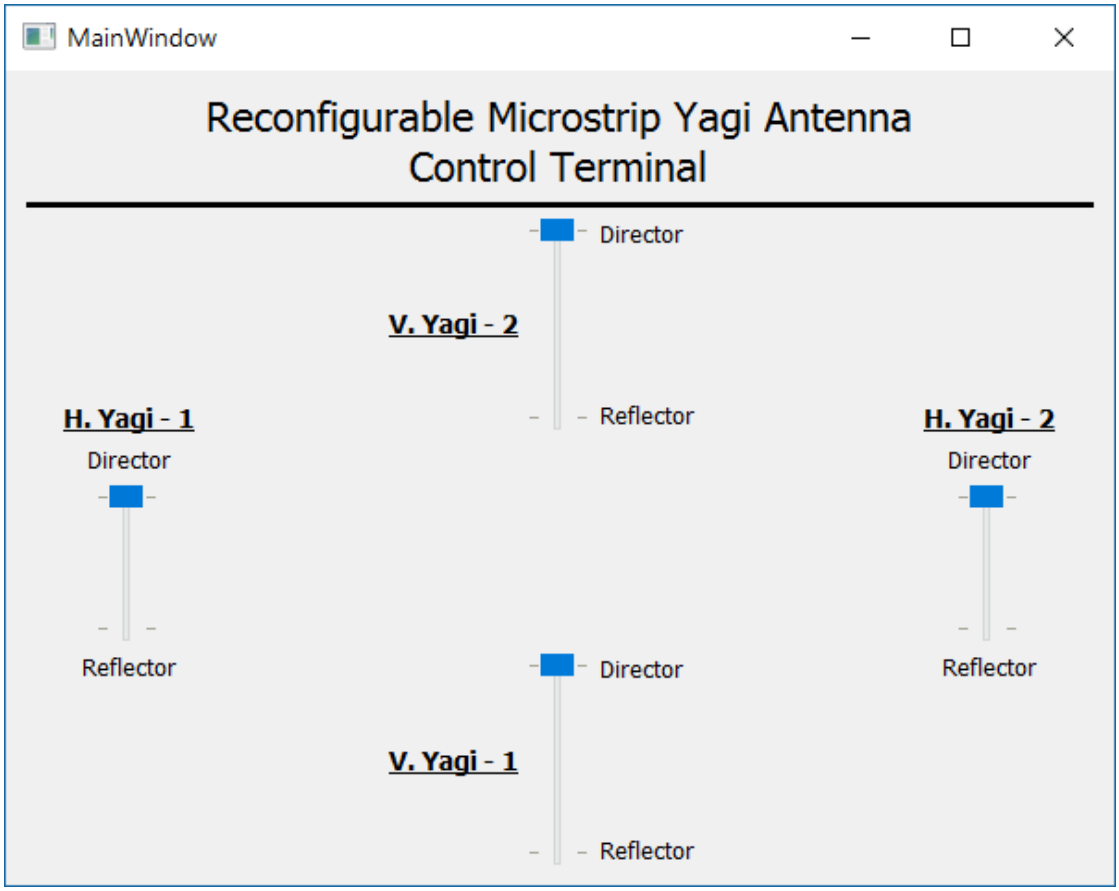

Fig. 48. Screenshot of the modified version of the software program for the reconfigurable ARMSP antenna.

While the antenna in [2] and [3] was able to switch polarization states electronically, this antenna uses the same mechanism to achieve pattern reconfiguration. Initial design states of the antenna had two diode bias states on each Yagi element, while final stages had three diode bias states. In the final design, the biasing of one Yagi element required the knowledge of the Yagi element on the opposite side. This knowledge required to be abstracted from the end-user and was this implemented in the software program, maintaining the same GUI, with modifications made only to the software application running on the back-end

CHAPTER VII

FUTURE WORK AND CONCLUSIONS

The antenna discussed in this thesis supports multiple polarizations but the feeding network was not mentioned. To achieve this, a software controlled Butler-matrix with digital phase shifters will be designed and implemented as a plug-and-play device as part of future work.

Adding a greater number of RF PIN diodes reduces the efficiency of the antenna due to losses in the diodes (additional series resistance, shunt capacitance and packaging inductance). It was stated that the length of the director needed to be adjusted to switch from DR or RD mode to DD mode and vice versa. This is intended to be achieved using varactor diodes, which enable a control over capacitance, thus allowing for an increase or decrease in the electrical length of the element. This is also intended as part of future work.

This this proposes a compact pattern and polarization reconfigurable microstrip patch antenna with capabilities of fast switching, with support for applications in the 2.4 GHz Wi-Fi band. A dual-probe feed approach was used to allow polarization reconfiguration. Several parasitic elements were strategically designed and placed around the antenna in order to achieve pattern reconfiguration. Adding reconfigurable parasitic elements allows for having a compact beam-steering antenna without the need for phase shifters or amplifiers.

REFERENCES

[1] K. B. Kaveripuram Ramasamy, "A Programmable MAC based System for Real-Time and Non-Real-Time Flows in Wireless Networks," Master of Science, Computer Engineering, Texas A&M University, College Station, TX, 2017 (unpublished).

[2] J. D. Barrera and G. H. Huff, "A Fluidic Loading Mechanism in a Polarization Reconfigurable Antenna With a Comparison to Solid State Approaches," *IEEE Transactions on Antennas and Propagation,* vol. 62, no. 8, pp. 4008-4014, 2014.

[3] J. D. Barrera, "Fluidic, Solid-State, and Hybrid Reconfiguration Techniques in a Frequency and Polarization Reconfigurable Antenna," Doctor of Philosophy, Electrical Engineering, Texas A&M University, College Station, TX, 2014.

[4] S. Zhang, "A Pattern Reconfigurable Microstrip Parasitic Array: Theory, Design, and Applications," Doctor of Philosophy, Electrical Engineering, University of Illinois at Urbana-Champaign, Urbana, IL, 2005.

[5] S. Zhang, G. H. Huff, J. Feng, and J. T. Bernhard, "A pattern reconfigurable microstrip parasitic array," *IEEE Transactions on Antennas and Propagation,* vol. 52, no. 10, pp. 2773-2776, 2004.

[6] R. E. Collin, *Foundations for Microwave Engineering*. Wiley, 2001.

[7] C. A. Balanis, *Antenna Theory: Analysis and Design,* 4 ed. Wiley, 2015.

[8] K. F. Lee and J. S. Dahele, "Theory and experiment on the annular-ring microstrip antenna," *Annales des Télécommunications*, journal article vol. 40, no. 9, pp. 508-515, September 01 1985.

[9] Y. Lo, D. Solomon, and W. Richards, "Theory and experiment on microstrip antennas," *IEEE Transactions on Antennas and Propagation*, vol. 27, no. 2, pp. 137-145, 1979.

[10] W. F. Richards, Y. T. Lo, and D. D. Harrison, "Improved theory for microstrip antennas," *Electronics Letters*, vol. 15, no. 2, pp. 42-44, 1979.

[11] R. B. Waterhouse, "Design of probe-fed stacked patches," *IEEE Transactions on Antennas and Propagation*, vol. 47, no. 12, pp. 1780-1784, 1999.

[12] Skyworks, "Data Sheet: SMV1405 to SMV1430 Series: Plastic Packaged Abrupt Junction Tuning Varactors," Available: www.skyworksinc.com, 2016.